

On the SEDs of passively heated condensed cores

Jörg Fischera^{1,2}

¹ Research School of Astronomy & Astrophysics, Mount Stromlo Observatory, Cotter Road, Weston Creek, ACT 2611, Australia

² Canadian Institute for Theoretical Astrophysics, University of Toronto, 60 St. George Street, ON M5S3H8, Canada

Preprint online version: June 3, 2018

ABSTRACT

Aims. The dust emission spectrum and the brightness profile of passively heated condensed cores is analyzed in relation to their astrophysical environment. The model is used to study systematically the radiative transfer effects on essential parameters such as the dust emissivity, dust temperature, and luminosity of the cores and to derive uncertainties in typical estimates of the IR flux and size.

Methods. The cores are modeled as critically stable self-gravitating spheres embedded at the center of self-gravitating filaments that are assumed to be either spherical or cylindrical in shape. The filaments are heated by an isotropic interstellar radiation field (ISRF). The calculations are based on a physical dust model of stochastically heated grains of diffuse interstellar dust. The spectral energy distribution (SED) of the cores is calculated using a ray-tracing technique where the effects of scattered emission and re-heating by dust grains are accurately taken into account. To compare with observational studies, the dust re-emission spectrum is approximated by a modified black-body function and the brightness profile with a Gaussian source. A simplified single-zone model for cores is presented that incorporates on the basis of the derived emissivities a first order approximation of their SED.

Results. Colder dust temperatures are, independent of the core mass, related to a higher pressure both inside and around the filament. The pressure-temperature relation for given external pressure is found to be largely independent of the true shape of the filament. The calculations show that the radiative transfer leads to a lower emission coefficient at $250 \mu\text{m}$ and to a flatter emissivity law of typically $\beta < 1.8$ in the far-infrared sub-millimeter regime. These effects cause the core mass to be underestimated by more than a factor of 2 based on the typical assumptions used in observational programs. A larger uncertainty is expected for high pressure regions. Fitting the core using a Gaussian source approximation overestimates the flux by $\sim 10\%$. For highly embedded cores and in general for cores in high pressure regions, the surface brightness profile is flatter with respect to the profile of the column density and a Gaussian profile. These effects can lead to an overestimate of the core size of 10 – 30% based on marginally resolved $250 \mu\text{m}$ observations.

Key words. Radiative transfer, ISM:dust, extinction, ISM: clouds, Infrared: ISM, Submillimeter: ISM

1. Introduction

Condensed cores are compact dense regions of molecular clouds that have a high column density contrast to their surrounding medium. They are regions of star formation and appear to be physically very similar to Bok-globules (Bok & Reilly 1947), dense, almost spherically shaped, highly compact molecular clouds surrounded by non-molecular thin interstellar gas (Curry & McKee 2000).

The formation of the condensed cores is potentially linked to the turbulent motion of the molecular gas that produces a self-similar multi-fractal density structure with a log-normal distribution of the local density. In this scenario, the cores are formed out of massive density enhancements that became self-gravitating and stable against the turbulent motion. Turbulence naturally produces a mass distribution of clouds similar to that observed in the ISM and is understood to be the origin of the initial mass function (IMF) of the stars (see references in Fischera & Dopita (2008)).

Because the cores are highly opaque, they are most easily studied in the far infrared (FIR) or submm regime by observing the dust emission spectrum where the cores are still optically thin. Surveys of molecular clouds performed in the

FIR/submm (as are possible using BLAST, HERSCHEL, and ALMA) are essential to our understanding of the very early evolutionary process of star formation and will help us to unlock the mystery of the origin of the IMF (e.g. Netterfield et al. (2009); Olmi et al. (2009)). The interpretation, however, of the dust emission spectrum is complicated by both radiative transfer effects and the unknown dust properties in the molecular phase of the ISM. Both effects lead to uncertainties in particular in the measurement of the core masses, which is the main observable derived by modeling the SED. This causes a major problem in gaining information about the efficiency of star formation, the stellar mass, or the masses produced within a core of a certain mass. The radiative transfer also further affects the surface brightness profile of the core as grains in the cloud are heated by a gradually changing radiation field (Fischera & Dopita 2008; Nutter et al. 2009).

Observationally, cores display, if described by a single temperature model, a large variation in dust temperatures. This is a direct consequence not only of their gravitational state, but also of their local environment. Some cores are exclusively heated by an external radiation field while others have already formed a protostellar object in the center

and are therefore also heated from the inside. Cores with a warm central object therefore have on average a higher dust temperature (Olmi et al. 2009).

The SEDs of interstellar clouds and cores have been extensively studied in the past (Bernard et al. 1992, 1993; Evans et al. 2001; Stamatellos & Whitworth 2003; Stamatellos et al. 2004; Fischera & Dopita 2008), although with different emphases. Bernard et al. (1992) studied the radiative transfer using a physical dust model and derived the brightness profiles and SEDs of interstellar clouds while making simplified assumptions about the scattered light and density profiles in clouds (a flat center and a power law further out). They concluded that the observed brightness profiles cannot be caused by radiative transfer effects alone. Evans et al. (2001), Stamatellos & Whitworth (2003), and Stamatellos et al. (2004) studied the infrared emission from cores to obtain more robust estimates of their dust masses. Their calculations focused on the radiative transfer aspects and used a simplified dust re-emission model based on the mean dust properties that they adopted from Ossenkopf & Henning (1994). Fischera & Dopita (2008) studied the dependence of the SED derived for stable isothermal self-gravitating interstellar clouds on the radiation field and the external pressure in the interstellar medium. These calculations were based on a physical dust model of interstellar dust grains. The radiative transfer problem was solved by accurately considering the complications caused by the scattered light to provide (as can also be found in the work of Stamatellos & Whitworth (2003)) profiles of the surface brightness for the whole SED.

Stamatellos & Whitworth (2003) studied the SEDs of cores embedded in optical thick dense spherical clouds and the present work can be compared to theirs. There are, however, basic differences. In their model, the giant molecular cloud (GMC) is not modeled as a self-gravitating entity but as a homogeneous dense sphere and the pressure inside the GMC is assumed to be independent of the extinction of the cloud.

In this paper, I relate the SEDs of passively heated condensed cores to their physical environment. The calculations rest upon comparable studies of interstellar clouds that are either spherical (Fischera & Dopita 2008) or cylindrical (Fischera, in prep.) in shape and are modeled as self-gravitating entities. As a first approach, I focus on the radiative transfer effects and base the SEDs of the cores on dust properties in the diffuse ISM. Complications caused by the turbulent density structure of molecular clouds are not considered and additional studies will be needed to quantitatively understand how the results presented in this paper are affected. The expected effects are discussed.

To compare the results with observations, the dust re-emission spectrum is described by a modified black-body spectrum. This provides the corresponding observational parameters of the dust emissivity and dust temperature. On the basis of these effective values, I present a luminosity-temperature relation and a pressure-temperature relation of embedded cores. I compare the surface brightness with a Gaussian function that is used observationally to extract the fluxes and the size of the cores (Olmi et al. 2009; Netterfield et al. 2009).

In Sect. 2, I present my model of passively heated embedded cores, the dust model, and the technique used to solve the radiative transfer problem. I also provide for comparison with observational data a single zone model. My

results of the radiative transfer calculations are presented in Sect. 3.1. In Sect. 3.2, I compare my model with the modified black-body spectrum and in Sect. 3.3 I provide the surface brightness. In Sect. 4, I discuss the effect of my results on uncertainties in the radiation field and dust properties, and provide a summary of the main results of the paper in Sect. 5.

2. Model

2.1. Model of embedded cores

2.1.1. Model of the cores

The cores are modeled as isothermal self-gravitating spheres, so-called Bonnor-Ebert spheres (Ebert 1955; Bonnor 1956), which are embedded in extended molecular clouds and pressurized by its central pressure p_c (see references in Fischera & Dopita (2008)). The cores are naturally in different gravitational states. However, for simplicity I consider in this work the cores that are in the critical state against collapse.

As described in Curry & McKee (2000) or Fischera & Dopita (2008), critical stable clouds are characterized by a steep density profile at the outskirts close to $1/r^2$, that becomes flat at the cloud center. They have an overdensity or overpressure \hat{p} of 14.04 in the cloud center where the overpressure \hat{p} is defined as the ratio of the pressure inside the cloud to the external pressure. Stable clouds are characterized by a flat density profile and lower overpressure, supercritical clouds by a steep density profile (also $1/r^2$) and higher overpressure. Observationally the cores are probably in a critical or super-critical state as they have a high column density contrast and are therefore easy to identify as individual sources.

The stability of a spherical isothermal self-gravitating cloud against gravitational collapse is determined by the temperature, the molecular weight, and the pressure outside the cloud. The temperature is considered as an effective value that contains, apart from the thermal motion, the turbulent motion of the dusty gas. In the critical state of the core, its mass is given by

$$M_{\text{core}} = 0.688 \left(\frac{T}{10 \text{ K}} \right)^2 \left(\frac{\mu}{2.36} \right)^{-2} \left(\frac{p_c/k}{2.8 \times 10^5 \text{ K/cm}^3} \right)^{-\frac{1}{2}} M_{\odot}, \quad (1)$$

where I have assumed that the pressure p_c at the center of the GMC is 14 times the mean pressure in the ISM of $p/k = 2 \times 10^4 \text{ K/cm}^3$ proposed by Curry & McKee (2000) and also adopted by Fischera & Dopita (2008). The cores are also assumed to be molecular, which implies a mean atomic weight of $\mu \approx 2.36$. The cores' radius simply scales with the temperature and is given by

$$R_{\text{core}} = 0.0345 \left(\frac{T}{10 \text{ K}} \right) \left(\frac{\mu}{2.36} \right)^{-1} \left(\frac{p_c/k}{2.8 \times 10^5 \text{ K/cm}^3} \right)^{-\frac{1}{2}} \text{ pc}. \quad (2)$$

In higher pressure regions, cores of the same temperature are more compact, have higher density, and are less massive. Combining both of these properties provides the mass-radius relation for cores

$$M_{\text{core}} = 5.78 \left(\frac{R_{\text{core}}}{0.1 \text{ pc}} \right)^2 \left(\frac{p_c/k}{2.8 \times 10^5 \text{ K/cm}^3} \right)^{\frac{1}{2}} M_{\odot}. \quad (3)$$

Of prime importance to the radiative transfer calculations is the optical depth through the cloud and its density profile. The column density through the cloud center for a given gravitational state is reflected by the density profile or overpressure is, independent of the true mass, determined by the pressure surrounding the cloud. For a critically stable cloud, the column density is, assuming solar abundances, given by the expression

$$N_{\text{H}}(0) = 5.8 \times 10^{22} \sqrt{\frac{p_{\text{c}}/k}{2.8 \times 10^5 \text{ K/cm}^3}} \text{ cm}^{-2}. \quad (4)$$

The column density through the center is difficult observationally to measure where the mean column density is instead derived. The corresponding mean column density of the critical stable core is then given by

$$\langle N_{\text{H}} \rangle = \frac{2}{3} \langle N_{\text{H}} \rangle (0) = 1.6 \times 10^{22} \sqrt{\frac{p_{\text{c}}/k}{2.8 \times 10^5 \text{ K/cm}^3}} \text{ cm}^{-2}, \quad (5)$$

where $\langle N_{\text{H}} \rangle (0)$ is the column density at the center of a cloud whose mass is distributed homogeneously inside the cloud volume (see Appendix B.1).

In higher pressure regions, cores of the same effective temperature are less massive, smaller, but more optically thick. In higher pressure regions, the dust inside the core is heated by a more strongly attenuated radiation field. For the same radiation field heating the core, the dust temperatures of the cores in high pressure regions are therefore colder than the cores in low pressure regions.

2.1.2. Model of the filaments

As the cores, the filaments are modeled as isothermal self-gravitating clouds surrounded by a thin interstellar medium of pressure p_{ext} . For comparison, both spheres and cylinders are considered as approximations of the observed structures in the ISM. As self-gravitating entities, they display a density and pressure profile.

It is reasonable to assume that condensed cores form out of density enhancements at the centers of the GMC. Here, potential cores experience the highest pressures and are therefore the locations where clouds can most easily become self-gravitating. Only those cases are therefore considered in the model. For simplicity, the mass and size of the core is assumed to be negligible to the mass and the extension of the filaments.

The physical properties of a critical stable spherical GMC is described by the same equations as given for the cores (Eq. 1 - 5). Replacing the pressure by the mean ISM pressure of $2 \times 10^4 \text{ K/cm}^3$, the mass radius relation is in good agreement with observations of interstellar molecular clouds (Larson 1981).

To study the whole range of structures from Bok-globules to highly embedded cores, I consider for a given external pressure different extinction values through the filaments. Since the central pressure of self-gravitating clouds is related to the column density at its center, the central pressure is also varied. The relation for spheres and cylinders embedded in the ISM of our Galaxy is shown in Fig. 1. For the same central extinction of a filament, cores situated in cylinders are subject to a higher central pressure than cores in spheres.

The range of extinction values considered in the paper leads to the situation indicated in Fig. 1, where the gravitational state of the spherical filaments varies over a wide range from highly stable to, in some cases, highly supercritical clouds. For the physical solutions of self-gravitating isothermal cylinders, a similar stability classification as for spheres does not exist as the cloud can always produce by compression a higher gas pressure at the cloud edge. The cylindrical filaments can therefore for all cases studied in the paper be regarded as stable.

Cylinders have a maximum mass-line density given by $M_{\text{cyl}}/L = 2K/G$, where M_{cyl} is the cloud mass, L is the cloud length, and G is the gravitational constant. The constant K , given by $k_{\text{B}}T/(\mu m_{\text{u}})$, is the one generally introduced in isothermal cloud models where k_{B} is the Boltzmann constant, m_{u} the atomic mass unit, and μ the mean molecular weight. This mass-line density is only reached in the limit of infinite overpressure (Fischera, in prep.). By construction, the mass-line density of cylinders with finite overpressure is lower than the asymptotic value. If we consider two clouds with the same mass-line density, a higher overpressure corresponds to a lower (effective) gas temperature. A change in the external pressure clearly has no consequence on the overpressure.

The situation is fundamentally different for spherical clouds where the maximum mass is identical to the critical stable mass given by $M_{\text{sph}} \propto (T/\mu)^2/\sqrt{p_{\text{ext}}}$, where a higher external pressure will change the gravitational state and can make the cloud unstable. While a cooling of a spherical cloud will consequently lead to a critical and finally unstable cloud it will lead only to a higher gravitational but still stable state in the case of cylinders. I note that - although a supercritical spherical cloud can be constructed - this state can not be obtained by means of simple cooling. If pressure equilibrium between cloud and the surrounding medium were assumed cooling of a critical stable cloud would lead to a *decrease* in the pressure at the outskirts. A spherical super-critical cloud assumed to be in pressure equilibrium with the surrounding medium also corresponds to a cloud temperature *above* the critical temperature (Fischera, in prep.).

Cylindrical self-gravitating clouds of high overpressure are characterized by a steep density profile at the outskirts with $\rho \propto r^{-4}$ (Stodólkiewicz 1963; Ostriker 1964). The observed density profile of interstellar clouds as pointed out by Fiege & Pudritz (2000a) appears to be less steep and more closely represented by a profile $\rho \propto r^{-2}$. Instabilities may explain these results as e.g. discussed by Larson (1985) or Fiege & Pudritz (2000b), which prevent the clouds producing high overpressures. However, cases with high overpressure are still useful in the framework of the radiative transfer problem and are therefore included in the model.

The column density at the center of self-gravitating cloud models is given by

$$N_{\text{H}}(0) = \frac{2}{m_{\text{u}} \sum_i \frac{n_i}{n_{\text{H}}} \mu_i} \sqrt{\frac{p_{\text{c}}}{4\pi G}} \int_0^{z_{\text{cl}}} dz e^{-\omega(z)}, \quad (6)$$

where ω is the potential, G the gravitational constant, μ_i the weight of element i in units of atomic mass units m_{u} , and z_{cl} is determined by the pressure equilibrium between the cloud and the surrounding medium $p(z_{\text{cl}}) = p_{\text{c}} e^{-\omega(z_{\text{cl}})} = p_{\text{ext}}$. The column density at the center of a

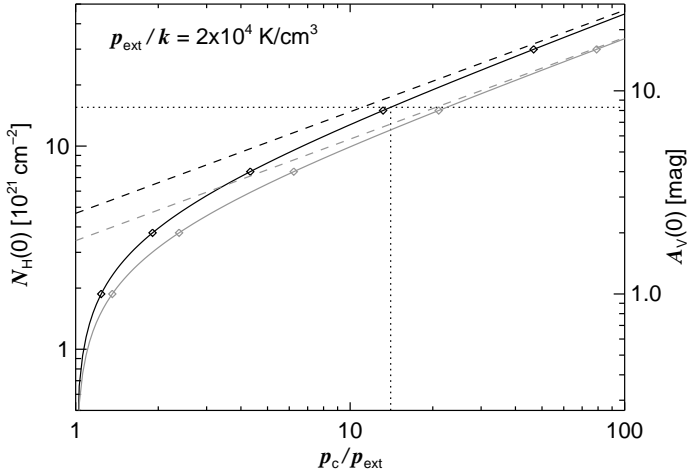


Fig. 1. Column density at the center of a spherical (black) and cylindrical (grey) isothermal self-gravitating cloud as a function of the overpressure p_c/p_{ext} , where p_c is the central pressure and p_{ext} is the external pressure. The dashed lines indicate the asymptotic behavior for high overpressure where $N_{\text{H}}(0) \propto \sqrt{p_c}$. The external pressure is assumed to be consistent with the mean pressure of $2 \times 10^4 \text{ K/cm}^3$ in the ISM of the Milky Way (Boulares & Cox 1990). The grey dotted lines show the values for a critical stable sphere with an overpressure of 14.045. The diamonds mark the values considered in the paper and correspond to $A_V = [1, 2, 4, 8, 16]$, where the extinction A_V is derived from the column density using the dust-to-gas ratio $E(B - V)/N_{\text{H}} = 5.8 \times 10^{-21} \text{ mag/cm}^{-2}$ (Bohlin et al. 1978) and the absolute to relative extinction $R_V = 3.1$ (Fitzpatrick 1999).

core given in Eq. 4 is a special case. In the limit of high overpressure, the integral in Eq. 6 becomes a constant and the column density solely a function of the central pressure p_c . The asymptotic behavior is given by

$$N_{\text{H}}(0) \sim 1.5 \times 10^{21} \xi \sqrt{\frac{p_c/k}{2 \times 10^4 \text{ K/cm}^3}} \text{ cm}^{-2}, \quad (7)$$

where

$$\xi = \int_0^\infty dz e^{-w(z)} = \begin{cases} 3.0279 & (\text{spheres}), \\ 2.2214 & (\text{cylinders}). \end{cases} \quad (8)$$

Because of this characteristic, in the case of high overpressure, the radiative transfer problem and as a consequence the dust temperature of the cores become largely independent of the external pressure.

2.2. Dust model

The dust is assumed to be a specific composition of graphites, silicates, iron grains, and PAH molecules where each dust component has a given size distribution. I use the same dust model parameters as Fischera & Dopita (2008), which were chosen to reproduce the observed dust properties of the diffuse phase of the ISM including the mean extinction curve (Fitzpatrick 1999), the diffuse dust emission derived with the DIRBE experiment (Arendt et al. 1998), and the depletion of key elements from the gas phase.

The dust re-emission spectrum and the PAH emission spectrum are derived by taking into account the stochastic

nature of the heating process for individual grains. This heating process is of particular importance for small dust particles where the thermal energy is typically lower than the absorbed photon energy, leading to large temperature variations.

There are some differences between my model and that of Draine & Li (2007) as mentioned in Fischera & Dopita (2008). First, the dust albedo in the optical is lower; secondly, the emission at shorter wavelengths where the dust emission spectrum is supposedly dominated by stochastic emission is enhanced by additional iron grains; and thirdly, the graphite grains are restricted to relatively large sizes with radii larger than $0.01 \mu\text{m}$ to avoid any contribution to the extinction bump at 2200 \AA , which is entirely explained by PAH molecules. The dust-to-gas ratio in mass is $\eta = 0.59\%$. As the grains possibly accrete gas atoms or molecules, the dust-to-gas ratio might indeed be slightly higher.

2.2.1. Mean extinction coefficient at long wavelengths

At far infrared wavelengths, where most of the grain cooling occurs, the extinction is close to the absorption probability. The mean cross-section for extinction per hydrogen atom in the model is given by the sum over the different dust components and the integrations over the individual size distributions

$$\langle C_\lambda^{\text{ext}} \rangle / H = \sum_i \zeta_i \int da f_i(a) \pi a^2 Q_\lambda^{\text{ext}}(i, a), \quad (9)$$

where $Q_\lambda^{\text{ext}}(i, a)$ is the extinction coefficient at wavelength λ of a dust grain of radius a and composition i . The size distributions $f_i(a)$ are normalized such that $\zeta_i = n_i/n_{\text{H}}$ is the relative amount of a key element that is part of the dust composition i (see Fischera & Dopita (2008)). The same expression as Eq. 9 is used to determine the scattering cross-section and the absorption cross-section. The dust albedo is given by the ratio $\omega_\lambda = \langle C_\lambda^{\text{sca}} \rangle / \langle C_\lambda^{\text{ext}} \rangle$.

The mean cross-section for the dust extinction assumed in the model calculations is shown in Fig. 2. The values in the FIR/submm regime are close, albeit slightly lower, than the ones derived by Weingartner & Draine (2001). The behavior is predominantly determined by graphite, PAH, and silicate grains. The relative importance of the components changes as a function of wavelength. While the extinction in the optical is caused mainly by carbonaceous grains, silicate is the dominant absorber from $10 \mu\text{m}$ up to $60 \mu\text{m}$. In the FIR/submm regime, the extinction is caused almost in equal parts by silicate and graphite grains. The extinction curve at wavelengths above $40 \mu\text{m}$, in the spectral region where the bulk of the cold dust emission occurs, is approximated well by a power law. The extinction coefficient per unit mass is given by

$$\langle \kappa_\lambda^{\text{ext}} \rangle = \frac{\langle C_\lambda^{\text{ext}} \rangle / H}{\langle \rho_{\text{d}} \rangle / H}, \quad (10)$$

where

$$\langle \rho_{\text{d}} \rangle / H \approx 1.384 \times 10^{-26} \frac{\text{g}}{\text{H} - \text{atom}} \quad (11)$$

is the mean dust density per hydrogen atom (Fischera, in prep.). The long-wavelength behavior above $60 \mu\text{m}$ to

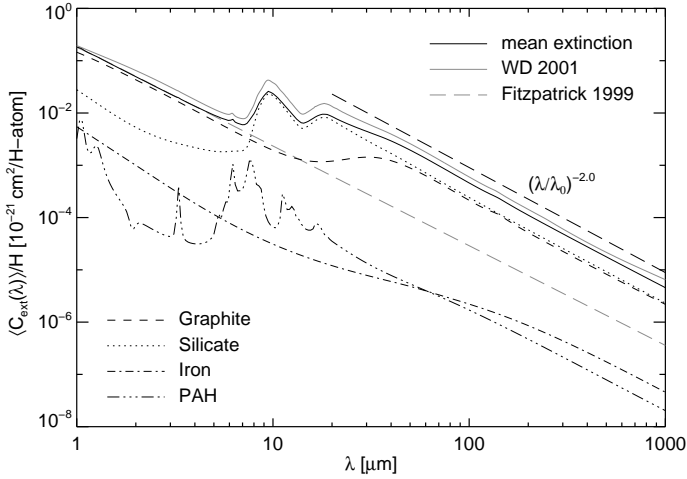


Fig. 2. Mean cross-section of the dust extinction per hydrogen atom as assumed in the radiative transfer model. Its functional dependence on wavelength is compared with the observed mean extinction for the diffuse ISM (Fitzpatrick 1999) (although extended to the FIR) and the mean extinction curve provided by Weingartner & Draine (2001) (corrected by a factor 0.93). Also shown are the contributions of the several dust components in the model.

1000 μm is (within 4% accuracy to the dust model) described by

$$\langle \kappa_{\lambda}^{\text{ext}} \rangle \approx 5.232 \left(\frac{\lambda}{250 \mu\text{m}} \right)^{-2.024} \frac{\text{cm}^2}{\text{g}}. \quad (12)$$

The power-law behavior of the dust model also extends to longer wavelengths. The approximation up to $10^4 \mu\text{m}$ is accurate to within 10%.

The extinction coefficient per unit length is $k_{\lambda}^{\text{ext}} = (\langle C_{\lambda}^{\text{ext}} \rangle / H) n_{\text{H}}$.

2.3. Radiative transfer

The filaments are assumed to be heated by an isotropic interstellar radiation field (ISRF) adopted from Mathis et al. (1982). The spectrum is characterized by a sharp cutoff at 13.6 eV and contains, apart from the stellar component, no re-emission from dust grains.

The radiative transfer is solved by assuming that the mass and size of the core is negligible compared to the mass and size of the filaments, the cores are embedded in. Under these circumstances the radiative transfer problem can be solved in two separate steps: The radiative transfer through the filament and the radiative transfer through the core. The centrally located cores are heated by the mean intensity $J_{\lambda}(0)$ at the center of the filaments derived for the filaments without cores. For simplicity, the radiation field caused by the attenuated ISRF, the scattered emission, and the thermal dust emission from the filaments is assumed to be isotropic.

For fixed dust properties inside the filaments and cores, the radiative transfer problem (and therefore the SEDs of the cores) is determined by the pressure of the gas surrounding the filaments and the overpressure p_c/p_{ext} in the filaments. The shape of the filaments has an additional effect on the radiative transfer because it determines the radial density profile, the extinction- central pressure relation

(Sect. 2.1.2) and the attenuation of the radiation inside the filaments. The influence of the shape of the filament on the SEDs of the cores is explored by considering both self-gravitating spheres and cylinders.

2.3.1. Accurate solution of the SEDs of the cores

For the given simplifications, the radiative transfer problem as a function of external pressure and overpressure is accurately solved using a ray-tracing technique (see Fischera & Dopita (2008)). This technique provides the angle-dependent radiation field inside the cloud caused by the attenuated radiation, the scattered radiation, and the thermal emission from dust grains. In the procedure, the cloud is divided into a number of optically thin shells. The impact parameters of the individual rays, which is their nearest distance to the cloud center, is given by the mean distance to the shells. For cylindrical geometric calculations, rays at 30 additional angles around the main rotation axis are considered (Fischera, in prep.). Effects caused by non-isotropic scattering and multiple scattering events are accurately included in the calculation as well as the effects of the re-heating of the dust grains and subsequent emission. The polarization of the scattered emission is assumed to have a negligible effect on determining the SED and is therefore ignored.

2.3.2. Approximate solution for the SEDs of embedded cores

When observations are analyzed, the dust re-emission spectrum of condensed cores is typically modeled by assuming a single dust temperature where the dust re-emission spectrum is approximated by a modified black-body spectrum. The SED (in units $\text{W}/\text{m}^2/\text{\AA}$) from the core of dust mass M_{dust} at distance D_{core} is given by

$$S_{\lambda}^{\text{dust}} = \frac{M_{\text{dust}} \kappa_{\lambda}^{\text{em}}}{D_{\text{core}}^2} B_{\lambda}(T_{\text{dust}}), \quad (13)$$

where T_{dust} is the dust temperature, $B_{\lambda}(T_{\text{dust}})$ the Planck-function, and $\kappa_{\lambda}^{\text{em}}$ the emission coefficient per unit dust mass. The emissivity is commonly approximated by a power law $\kappa_{\lambda}^{\text{em}} = \kappa_0 (\lambda/\lambda_0)^{-\beta}$ by making certain assumptions about the dust emissivity κ_0 at wavelength λ_0 and the power β (Netterfield et al. 2009; Olmi et al. 2009). The model is equivalent theoretically to a single-zone model for the dust temperature in the core. However, as shown in this paper, to obtain the correct shape of the dust re-emission spectrum and the correct dust mass, the intrinsic values of the dust emission coefficient need to be replaced by the appropriate effective values to take into account not only the variation in the emission spectrum with both size and composition but also the radial variation in the grain temperatures. I use this approximation to obtain for the given dust mass and theoretical SED the appropriate effective parameters.

The single-zone model allows us not only to interpret the observations but also to test efficiently a wider range of model parameters. It is therefore a more practical model to use than time-consuming ray-tracing calculations. The model is described in detail in Sect. A. In the approximate solution of the radiative transfer problem based on energy conservation the effects of both scattering and re-heating by dust grains inside the filaments and the cores are taken into

account. However, in the considered cases the contribution of self-absorption to the total heating rate inside the clouds is negligible. Of greater importance is the contribution of dust emission from the filaments to the total heating of highly embedded cores. In the model approximation this additional heating is provided as a lower limit.

3. Results

The dependence of the effective parameters is analyzed for three assumptions about the external pressure. Apart from the mean pressure in the ISM ($2 \times 10^4 \text{ K/cm}^3$), situations where the filaments are embedded in a higher pressure gas (10^5 and 10^6 K/cm^3) are also considered. For each considered value of external pressure, the SEDs of the cores are derived for a range of extinction values A_V at the center of the filaments. For both spherical and cylindrical geometries for the filaments, I considered the extinction values 0, 1, 2, 4, 8, and 16. For cores in spherical filaments, I also assumed higher extinction values (32 and 64 mag). In these calculations, the energy is conserved in all cases to better than 0.2%.

In the following section 3.1, I describe the individual steps of the radiative transfer calculations. The results obtained using a modified Planck-function are described in Sect. 3.2.

3.1. The theoretical dust emission spectrum

3.1.1. The mean intensity at the filaments' center

The first result obtained using the ray-tracing technique is the mean intensity at the center of the filaments. The relative contribution of the attenuated external radiation field, the scattered emission, and the re-emission from dust grains located in the filaments to the SED is shown in Fig. 3 for two extinction and pressure values. For the ISM pressure ($p_{\text{ext}}/k = 2 \times 10^4 \text{ K/cm}^3$), the extinction value $A_V = 8$ mag in the spherical filament is close to the value of a critical stable sphere with overpressure 13.2, while the higher extinction value, $A_V = 64$ mag, corresponds to a supercritical spherical cloud with high overpressure (68.25). In both cases, the clouds are characterized by a steep density profile in their outskirts. In the high pressure region ($p_{\text{ext}}/k = 10^6 \text{ K/cm}^3$), the high extinction value is close to the corresponding critical value ($A_V \sim 59$ mag), while the low extinction value corresponds to a sub-critical spherical cloud. The clouds in the high pressure region are characterized by flat or steep density profiles with low and high overpressures (1.30 and 16.38, respectively) at the cloud center (see table 1).

The SED of the center of the filaments is primarily determined by the radial extinction and in parts by the geometry. The effects caused by the radial density profile play only a minor role in particular for the dust re-emission spectrum. The properties are of importance for interpreting the dust re-emission from cores and are described in the following.

Because of simple geometric effects, the radiation is, for identical values of A_V , more strongly attenuated by cylindrical than spherical geometry. The strength of the scattered light that dominates the SED below its maximum depends to a certain degree on the shape of the filaments. For the considered high extinction values, most of the scat-

tered emission in the UV and optical is generated in a skin layer of the filament, so that the geometric effects produce a lower amount of scattered emission at the center of the cylinders. The situation is different at longer wavelengths where the clouds become optically thin and the probability of scattering events is higher in cylinders than spheres. Despite its low intensity for the cases shown in Fig. 3, the scattered light is responsible for approximately half of the dust heating in the filaments' center (Fischera & Dopita 2008).

At the high extinction values considered, the amount of PAH emission produced in the filaments is rather insensitive to the extinction value since most of the flux responsible for heating the molecules is absorbed. The emission originates mainly in a layer close to the surface where the UV and optical light most responsible for heating the molecules is strong. The radiation in this layer is more intense in low pressure regions causing for a given extinction a slightly stronger PAH emission at the filaments' center. In the case of $A_V = 64$ mag, the PAH emission itself experiences a certain extinction that is most evident in the larger minimum at $10 \mu\text{m}$, which is caused by silicate absorption. It can be seen overall, that the ratio of the PAH emission relative to the dust emission peak is considerably lower than in the diffuse ISM (Fig. 15).

The shape of the dust re-emission in the FIR/submm-regime depends for a given extinction and external pressure on the shape of the filaments. Radiation from cold dust grains located in the interior of the filament is higher in the case of a cylinder because of the infinite column density along the major axis. At relatively low extinction values ($A_V \sim 1$ mag) where the UV and optical light can penetrate deeper into the cloud, this also affects the intensity of the PAH emission and the warm emission of stochastically heated small grains. The dust emission peak at higher extinction values also appears to be broader because of the larger temperature variations and colder dust temperatures at the filaments' center.

3.1.2. Grain heating

The dust heating

$$h(r) = \int d\lambda (k_{\lambda}^{\text{abs}}/n_{\text{H}}) 4\pi J_{\lambda}(r) \quad (14)$$

at the core caused by the mean intensity in the filament varies strongly inside the core (as seen in Fig. 4) because the light, especially in the UV and optical, is strongly attenuated by dust scattering and dust absorption towards the core center. This radial variation is even stronger in the high pressure region ($p_{\text{ext}}/k = 10^6 \text{ K/cm}^3$), where cores experience higher pressure and are more opaque.

In Fig. 4, the heating is divided into several components corresponding to the various radiation fields inside the core. For cores in filaments with $A_V = 8$ mag, the heating is dominated almost in equal parts by the attenuated *ISRF* and the scattered light. As visible in the figure, inside the core the scattered radiation field is mostly caused by photons scattered inside the core. Deep inside highly opaque cores and in the case of highly embedded cores the scattered contribution decreases relative to the attenuated *ISRF* as the heating shifts to longer wavelengths where the dust albedo is lower.

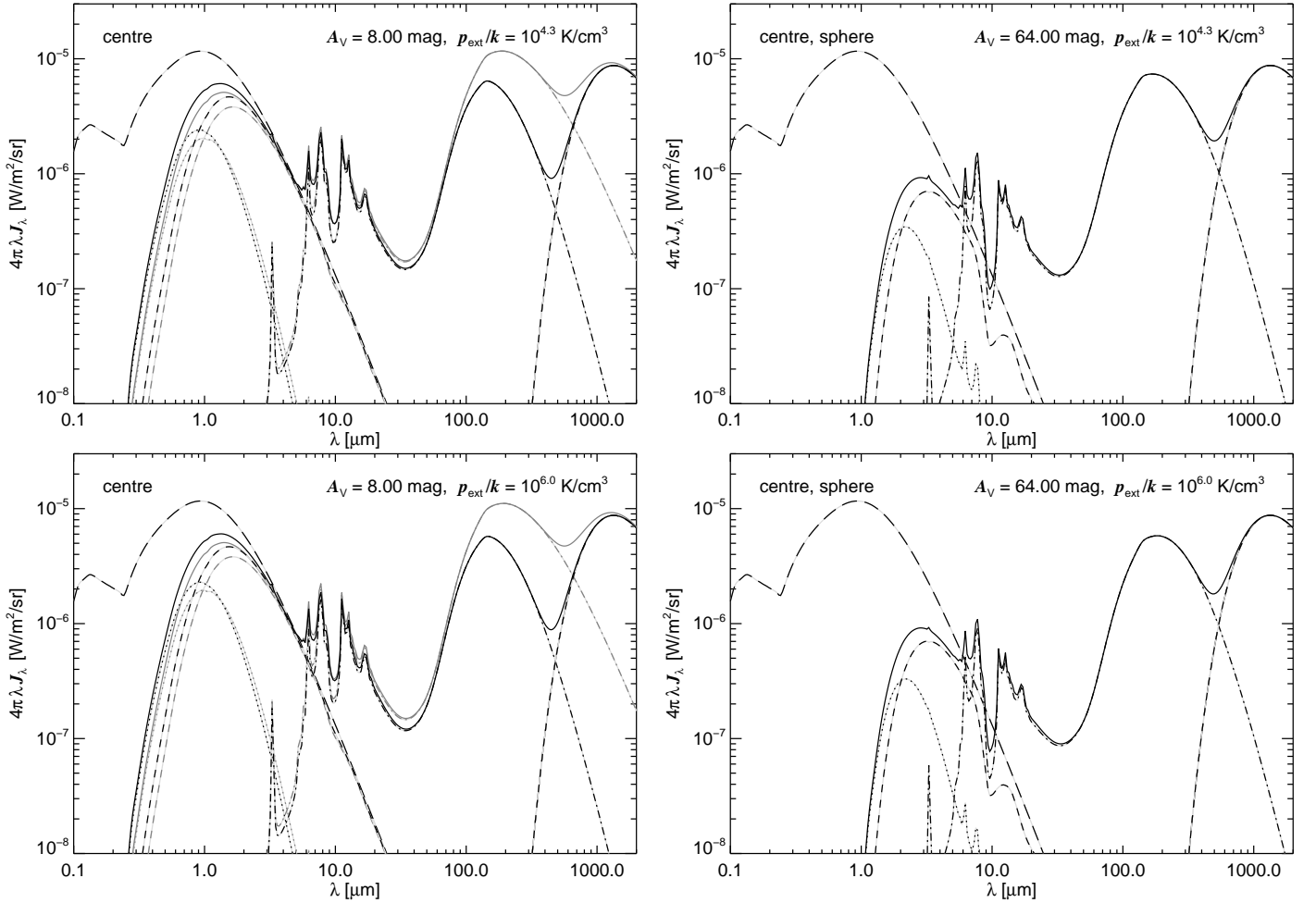


Fig. 3. Mean intensity at the center of spherical (black solid lines) and cylindrical (grey solid lines) filaments heated by the ISRF (long dashed lines). The filaments are embedded in a medium with $p_{\text{ext}}/k = 2 \times 10^4 \text{ K/cm}^3$ (top) and 10^6 K/cm^3 (bottom). The extinction through the filaments' center is either $A_V = 8 \text{ mag}$ (left-hand figure) or $A_V = 64 \text{ mag}$ (right-hand figure). Shown are the different components of the mean intensity: scattered emission (dotted lines), attenuated light (short dashed lines), and dust re-emission (dashed-dotted lines). The emission peak in the millimeter regime is the CMB radiation.

In case of a strongly attenuated external radiation field, the heating by dust emission from the filament and the core becomes an important component. This applies either for the central region of highly opaque cores and for highly embedded cores in general. The size of the contribution in reality depends certainly on the dust properties in the dense phase of the ISM. The heating derived here may be an upper limit since most of the heating is caused by the PAH emission which is possibly absent in realistic clouds. The heating by self-absorption plays a larger role in the case of non-embedded cores in high pressure regions (see Fischera & Dopita (2008)). For the considered cases in Fig. 4 of embedded cores, the contribution is smaller than $\sim 10\%$. Far more important is the heating caused by the dust emission from the filaments. At $A_V = 8 \text{ mag}$, this component produces at the center of the cores embedded in spherical filaments between 13% and 25% of the total heating rate. The contribution is even higher if the cores are instead embedded in cylinders (20 – 35%). For highly embedded cores, the dust in the whole interior of the cores is predominantly heated by the dust emission from the filaments. This additional heating limits the variation in the

heating rate inside the core. I note that the heating component is higher in the low pressure region.

The effect of the external pressure and the extinction of the filament on the temperature variation in the heating rate inside the core is further visualized in Fig. 5 where the heating rate in the center is compared with the heating rate at the cores' edge. For comparison with simplified radiative transfer models, the heating rate is also related to a dust temperature. The heating rates at the cores' edge are determined in a preliminary way for a given filament shape by the extinction A_V through the filaments' center. Since the cores are more compact for a given extinction in higher pressure regions that produce a lower intensity at the cores' edge, the heating rate decreases slightly to higher pressures. The effect reaches a maximum of only a factor of two. Clearly visible in the figure is the dependence of the overpressure on the extinction of the filaments for a given external pressure. While the overpressure changes drastically in the low pressure regions also in case of low extinction, the effect is small for filaments in high pressure regions.

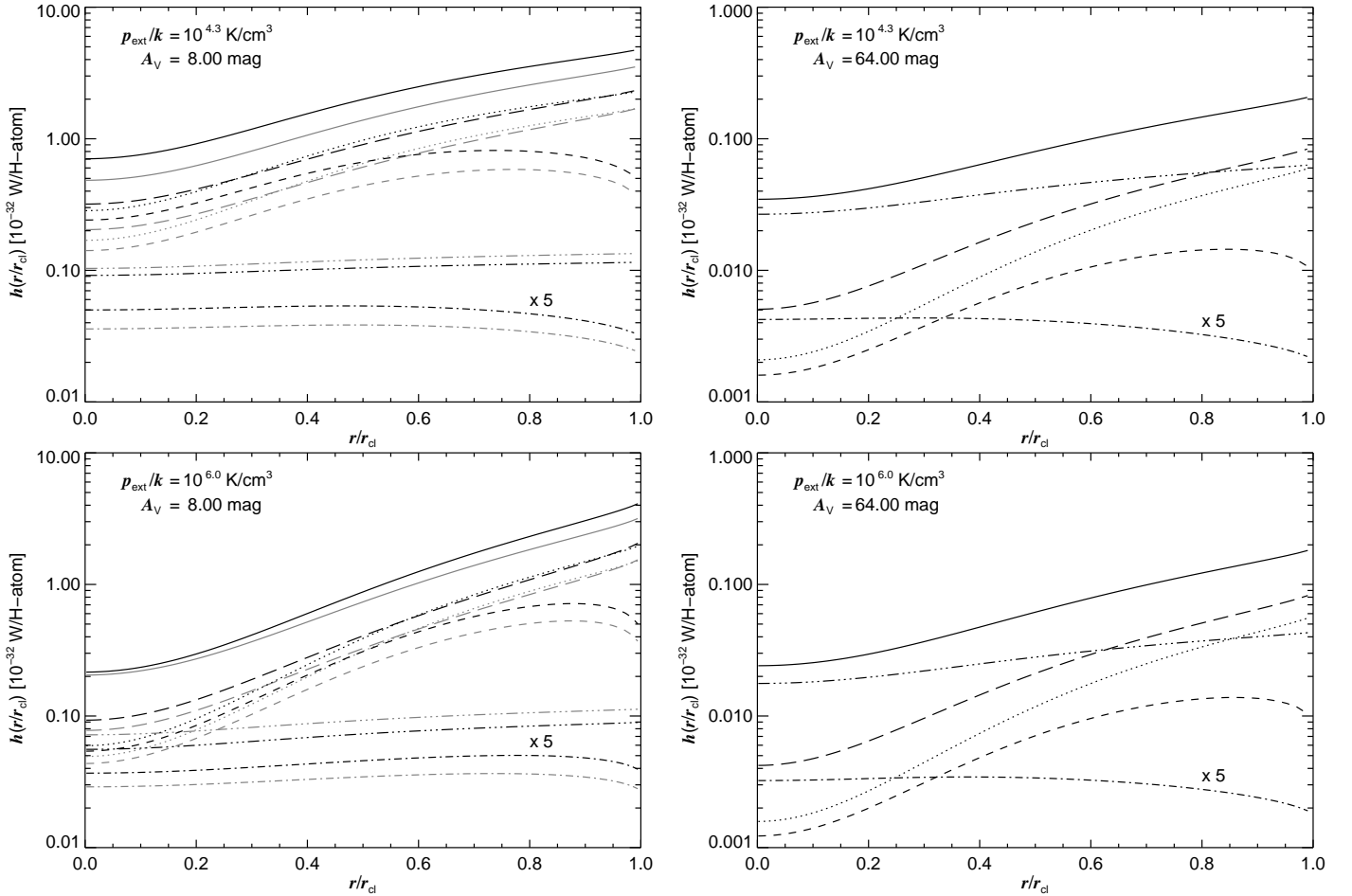


Fig. 4. Dust heating inside cores embedded in spherical (black curves) or cylindrical (grey curves) filaments. The visible extinction A_V at the center of the filaments is either 8 mag (left-hand figure) or 64 mag (right-hand figure). The filaments are pressurized either by the mean pressure in the ISM (top) or by a medium with $p_{\text{ext}}/k = 10^6 \text{ K/cm}^3$ (bottom). The total heating rates (solid curves) are separated into different components corresponding to the different radiation fields in the core: Attenuated *ISRF* (long dashed curves), total scattered light (dotted curves), light scattered in the core (short dashed curves), dust emission from the filament (dashed-three dotted curves), and dust emission from the core (dashed-single dotted curves). The heating by dust emission produced inside the core is multiplied by a factor 5.

The lowest dust temperature in the core is strongly dependent on the pressure surrounding the core, which determines its extinction. However, there are some noticeable systematic effects caused by the shape of the filament and the external pressure. At a certain pressure p_c , the minimum temperatures are naturally lower for embedded cores in low pressure regions p_{ext} than for non-embedded cores in high pressure regions. The behavior at high pressure values p_c for a given external pressure reflects the differences in the dust emission inside the filament noticeable in Fig. 4. For given external and internal pressures, the dust at the center of cores is for example slightly warmer, if they are embedded in cylindrical filaments as the intensity of the dust emission is higher in cylinders than in spheres.

As seen in Fig. 4, the qualitative behavior of the relative variation of the heating rate or the temperature inside the core depends on the pressure surrounding the filaments. In high pressure regions, the variation in the dust temperature inside the cores decreases if the core becomes more embedded and shielded from the *ISRF*. As the cores become more optically thin to the reddened radiation, the radial varia-

tion in the heating rate and consequently that of the dust temperature become smaller.

The situation in the low pressure region is more complex as the increase in the extinction of the filament is accompanied by a higher pressure at its center. The embedded cores are not only heated by a reddened radiation field but are also more opaque than non-embedded cores. Above $A_V = 1 \text{ mag}$, this leads, assuming a mean ISM pressure, to an increase in the dust temperature variation with central pressure. As will be shown this causes a flattening of the overall SED with extinction (Sect. 3.2.1). The variation in the dust temperature inside embedded cores is not necessarily lower than for non-embedded cores. Based on my calculation, the cores in molecular clouds of typical extinction $A_V = 8$ display even slightly larger temperature variations than non-embedded cores.

Independent of the assumed external pressure, the variation in the heating rate decreases for highly embedded cores within filaments with $A_V \gg 16 \text{ mag}$, where the interior of the cores becomes predominantly heated by the dust emission from the filaments.

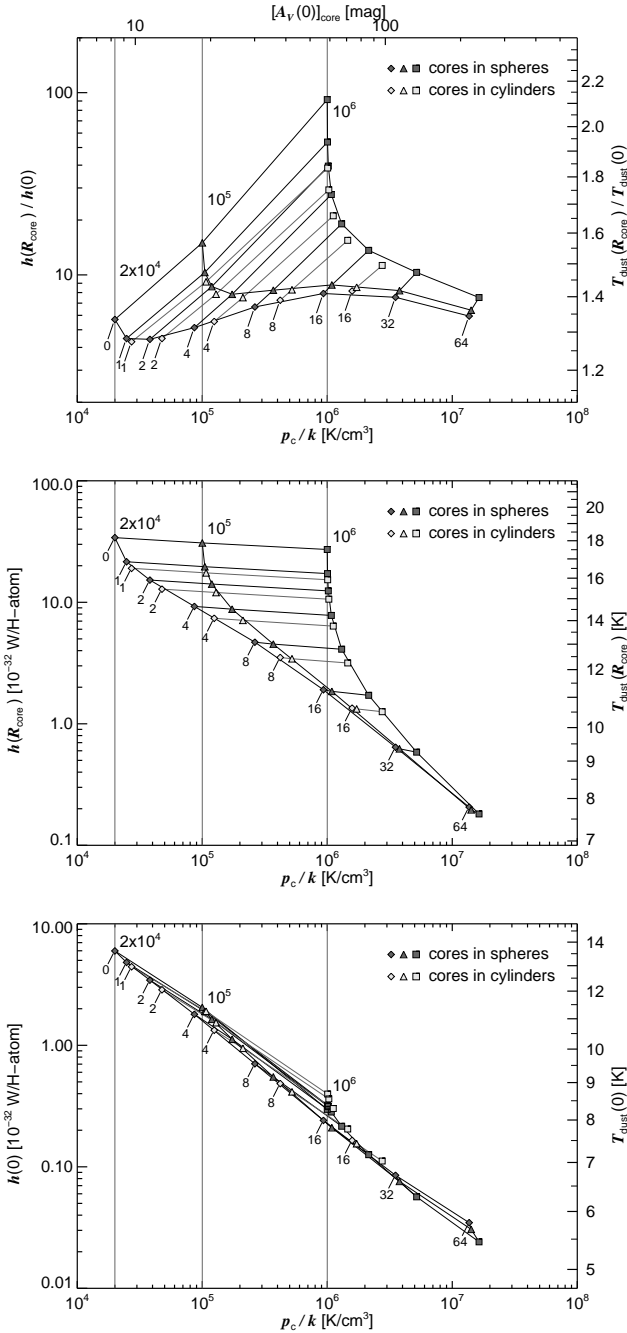


Fig. 5. Ratio $h(R_{\text{core}})/h(0)$ (top figure), the heating rate $h(R_{\text{core}})$ at the cores' edge (central figure), and the heating rate in the core center $h(0)$ (bottom figure) as a function of the central pressure in the filaments for the three different assumption of the external pressure p_{ext} . For comparison also the corresponding dust temperatures of a simplified dust model are shown. For sake of clarity the values obtained for cores in spherical filaments which are pressurized by the same external pressure p_{ext} are given as solid black curves. The values are labelled with the considered extinction values A_V through the filaments' center.

3.1.3. Grain temperatures

In the model, the SEDs of the cores are produced by the re-emission of individual grains of different sizes and compositions that have unique temperature and emission be-

haviors. The temperature of the individual grains as a function of radius is shown in Fig. 6. The grain sizes are large enough for their temperature distribution to be close to a narrow distribution around the equilibrium temperature. The radial variation in the temperature is most visible for the smallest grains, which are heated predominantly by the strongly diminished UV and optical light. The figure also shows the dependence of the dust temperature on composition. Small iron grains are considerably warmer than silicate or graphite grains because of the high absorption in the UV and optical and the low emission probability in the infrared (Fischera 2004). In cores embedded in filaments with $A_V = 8$ mag that are pressurized by the mean ISM pressure, the temperatures of large grains lie between 8 K and 15 K. I note that the temperature variation for different grain types is smaller in both the core interior and more opaque filaments where the grains are heated by a more reddened radiation field. The physical explanation is the similar absorption and emission behavior of the grains at long wavelengths, which for most grains is closely described by a power law with $Q_{\lambda}^{\text{abs/em}} \propto a/\lambda^2$ where a is the grain size. In this limit, the ratio of the cooling to the heating rates and therefore the grain temperatures become the same.

3.1.4. The SEDs from cores

Figure 7 shows the obtained SEDs of cores, which are embedded in spherical filaments with $A_V = 8$ mag and $A_V = 64$ mag. The SEDs of cores embedded in cylindrical filaments have the same properties but slightly lower PAH emission and lower dust temperatures for the same extinction values.

The SEDs reflect the dependence of the opaqueness of the cores on both extinction and external pressure as discussed in the previous sections. For highly embedded cores, the SEDs depend to most parts on the extinction of the filament and is largely independent of the external pressure (Sect. 2.1.2). The cores are highly opaque and are heated almost in equal part by the attenuated stellar radiation field and the PAH emission from the filaments (see Appendix A, Fig. A.1). The minimum around $10 \mu\text{m}$ is enhanced by silicate absorption.

At the blue side of the spectrum, the emission is dominated by light scattered within the core. For a given extinction A_V , the scattered radiation is only mildly dependent on the pressure since most of the scattered light originates in a layer close to the surface of the core (see Fig. 4). Multiple scattered light only becomes important at wavelengths $\lambda < 3 \mu\text{m}$.

The bulk of the dust re-emission is closely described by a modified black-body function. At shorter wavelengths, the spectral shape is dominated by the emission from stochastic dust emission, small grains, and PAH molecules. The effect of the dust attenuation inside the core is clearly visible in the PAH emission. Because of the low intensity of the UV/optical, the ratio of the PAH emission to the dust emission peak is lower than in the diffuse ISM or inside the filaments (Sect. 3.1.1) and decreases systematically with extinction (Fig. 8). For highly embedded cores, the reddened radiation affects the spectral shape of the PAH emission spectrum as the photons are not sufficiently energetic to heat the molecules to high temperatures.

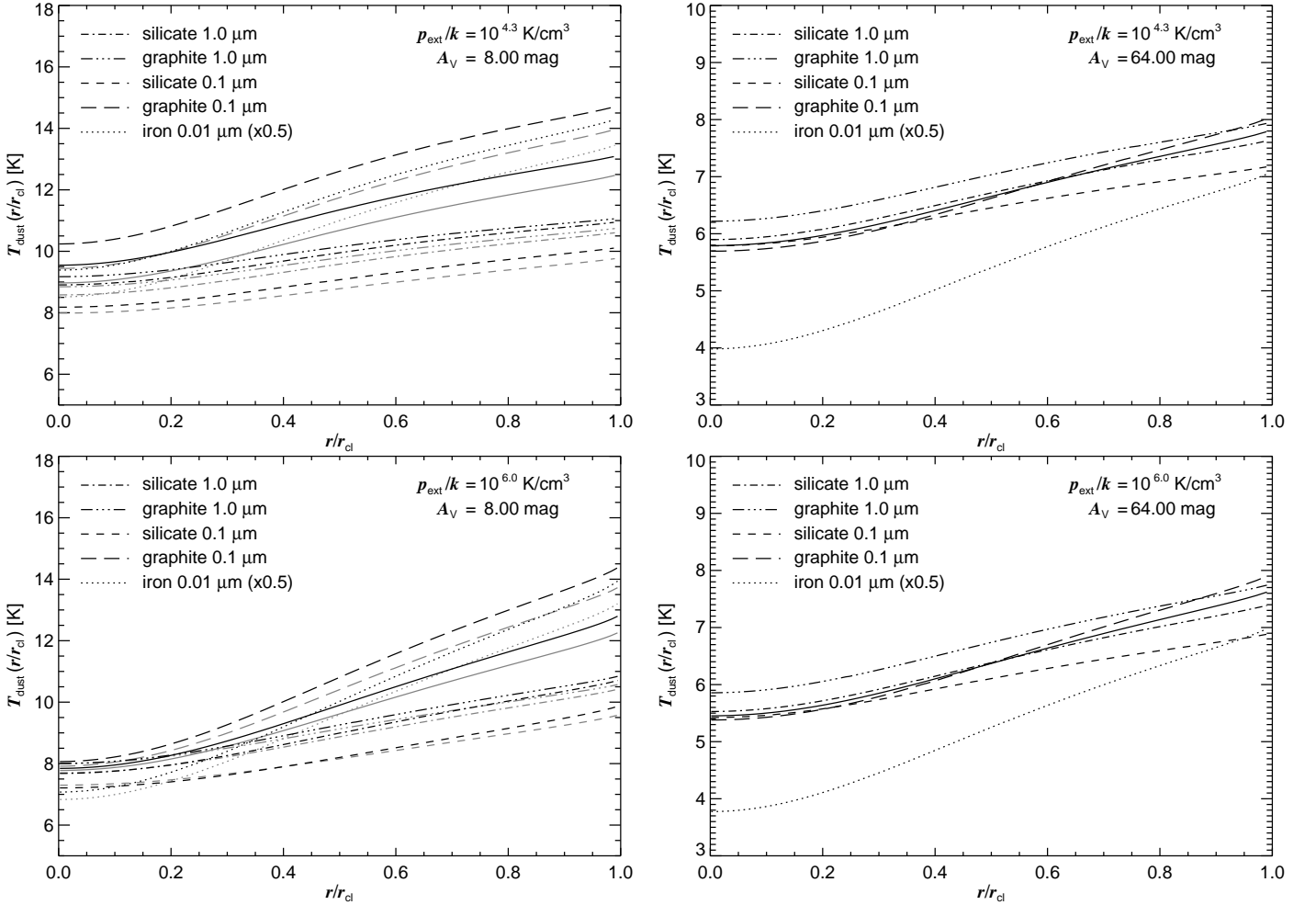


Fig. 6. Dust grain temperatures for a number of different sizes and dust compositions of cores embedded in spherical (black lines) or cylindrical (grey lines) filaments. The iron temperature is divided by a factor of 2. The effective values for a single temperature model of the dust grains is shown for comparison (solid curves) where the dust emissivity is approximated by a simple power law (Eq. 12). The external pressure p_{ext}/k outside the filaments is assumed to be either 2×10^4 (top) or 10^6 K/cm³ (bottom). The extinction through the filaments' center is either 8 mag (left-hand figure) or 64 mag (right-hand figure).

For a given extinction A_V , the PAH emission of embedded cores is not strongly dependent on the external pressure as the heating flux for the PAH molecules is largely absorbed in the core. The dust emission, on the other hand, appears to be colder and stronger in higher pressure regions as the grains in the core's center are heated by a more strongly attenuated radiation field with a larger fraction of the radiation being absorbed inside the core. There is, however, a limit to the total luminosity given by the *ISRF* heating the filaments (see Sect. 3.2.2)

The effect of the extinction for a given external pressure p_{ext}/k on the dust emission from cores is shown in Fig. 8, which covers the range from non-embedded (Bok-globules) to highly embedded cores. In low pressure regions, a higher extinction of the filaments leads to an enhanced emission in the Rayleigh-Jeans limit of the spectrum. This behavior is responsible for the pressure-extinction relation of the filaments. As I have shown (Sect. 3.1.2), this relation significantly decreases the heating rate inside the core and produces above $A_V \sim 1$ mag a larger temperature variation inside the core. The effect disappears if the extinction does not lead to a strong increase in the central pressure as in

the high pressure region below $A_V \sim 16$ mag. The lower amount of radiation from embedded cores is then largely compensated by the shift to colder dust temperatures.

3.2. The effective parameters for the SED

For direct comparisons with observations, the theoretical dust emission spectrum at long wavelengths is fitted by a modified black-body spectrum having T_{dust} , β , and κ_0 as free parameters. The fit is achieved using a non-linear χ^2 -fit with

$$\chi^2(\kappa_0, \beta, T_{\text{dust}}) = \sum_i \frac{(F_{\lambda_i} - S_{\lambda_i}(\kappa_0, \beta, T_{\text{dust}}))^2}{F_{\lambda_i}^2}, \quad (15)$$

where F_{λ_i} and S_{λ_i} refer to the mean theoretical flux and the mean fitted flux of the modified black body spectrum (Eq. 13) over wavelength bins i , respectively.

As can be seen in Fig. 7, the dust emission spectrum at shorter wavelengths from the maximum deviates consider-

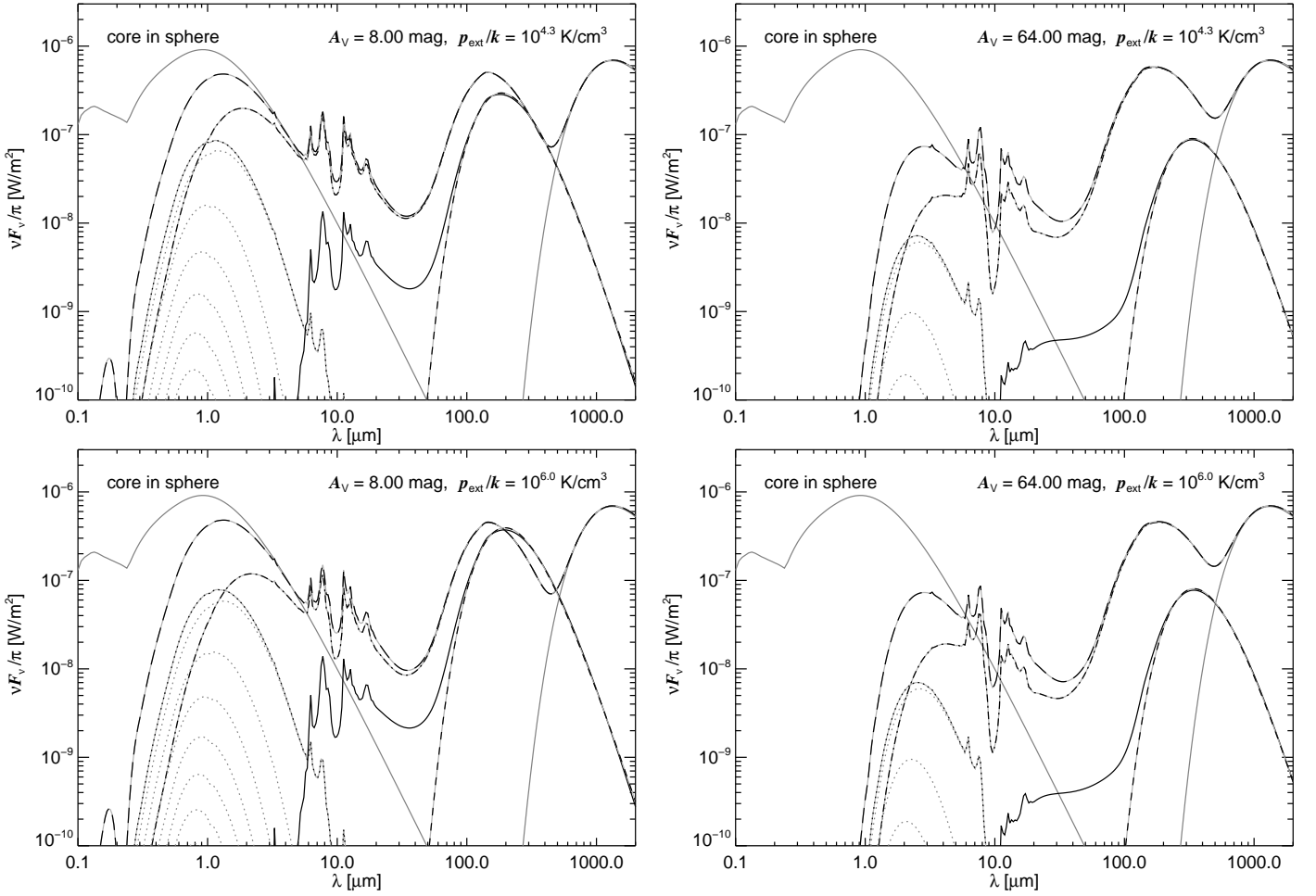


Fig. 7. SEDs of cores located at the center of a spherical filament with a total central extinction $A_V = 8$ mag (left-hand figure) and $A_V = 64$ mag (right-hand figure). The filaments are embedded in a medium with $p_{\text{ext}}/k = 2 \times 10^4$ K/cm³ (top) or 10^6 K/cm³ (bottom) and are heated by an unattenuated interstellar radiation field (grey solid line). The derived dust re-emission spectrum is shown as a solid black line, the radiation heating the core as a long dashed line, and the attenuated emission leaving the core as a dashed-dotted line. Also given is the emission produced by photons scattered inside the core (black dotted lines). The grey dotted lines show the individual components of multiply scattered photons. The top curve shows singly scattered emission, the curves below emission scattered twice and so on. The dust emission spectrum is fitted to a modified black-body function (short dashed line).

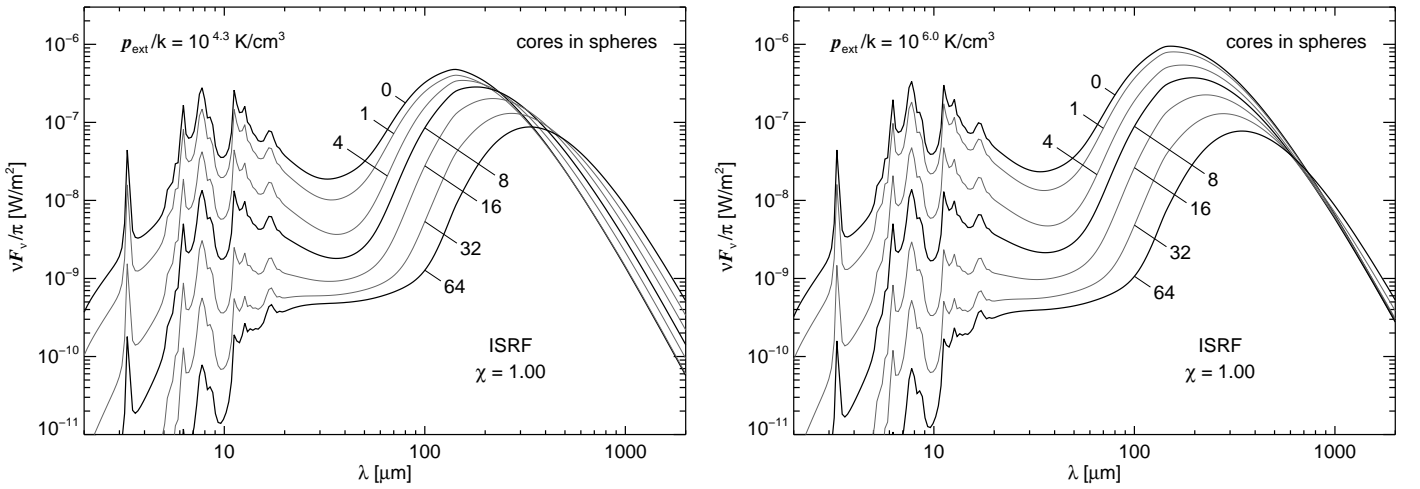


Fig. 8. SEDs of condensed cores embedded in the center of spherical self-gravitating filaments illuminated by the ISRF given by Mathis et al. (1982). The external pressure p_{ext}/k is either 2×10^4 (left-hand figure) or 10^6 K/cm³ (right-hand figure). The SEDs are labelled with the assumed extinction A_V through the filaments' center.

ably from the simple modified black-body spectrum. The fit is therefore restricted to the interval

$$[1400/T_{\text{dust}}[K], 10000] \mu\text{m}. \quad (16)$$

The derived parameters for the modified black-body approximation are listed in Table 1, where I also provide the luminosity of the modified black-body function and the integrated luminosity. In the model, at low extinction values, a larger fraction of the light is absorbed by PAH molecules and small dust particles and subsequently re-emitted at shorter wavelengths. This causes the modified black-body function to underestimate the total dust emission. The PAH/small dust particle contribution disappears gradually towards highly embedded cores as the UV and optical light becomes almost entirely absorbed inside the filaments heating the small dust particles. The last two columns give the *FWHM* and the total integrated flux of an Gaussian source approximation for the brightness profile (see Sect. 3.3). For β , κ_0 , L/M_{core} , and the *FWHM*, I provide polynomial fits as functions of the dust temperature (Table 2). I emphasize that the derived relations depend on the specific dust properties, and to an extent, on the radiation field. The relations provided are appropriate for dust with the properties of diffuse ISM dust.

As an estimate of the accuracy of the achieved fit, I list $\sqrt{1/\chi_{\text{red}}^2}$ where $\chi_{\text{red}}^2 = \chi^2/N_{\text{free}}$ and $N_{\text{free}} = N - 3$ is the number of free parameters. The accuracy is within 2.5% to 4% with the largest deviation occurring around the peak of the dust re-emission spectrum. The fit becomes worse for higher extinction values because of the larger temperature variations in the core. Closer agreement is achieved again at extinction values larger than $A_V = 64$ mag. Because of the larger temperature variations inside the core for a given central extinction of the filament, the agreement is also less good in high pressure regions. I note that in part the disagreement is also caused by the optical properties used in the radiative transfer calculations, whose properties differ, as those of graphite grains, strongly from a simple power-law behavior in the FIR.

In low pressure regions, the filaments and the condensed cores become less optically thin. In the limit of a very low pressure region, the dust emission from the cores is identical to the one in the diffuse ISM. To obtain the corresponding effective values of the modified black-body approximation for the diffuse dust emission, I considered a spherical self-gravitating cloud with $A_V = 0.01$ mag (assuming $p/k = 2 \times 10^4$ K/cm³).

The fit of the dust re-emission spectrum is not as good as for emission from the dense cores because the contribution of stochastically heated small grains at the blue side of the emission spectrum is stronger. The derived effective temperature is also at $T_{\text{dust}} = 19.86$ K relatively high. The parameters of the emissivity are $\beta = 1.83$ and $\kappa_0 = 3.40$ cm²/g.

If the grains are heated by the non-attenuated *ISRF*, the ratio of the luminosity of the dust emission to the total mass of gas and dust is close to ‘1’ (in solar units). The ratio obtained with the modified black-body fit is $0.736 L_{\odot}/M_{\odot}$. For the total dust emission spectrum, the ratio is higher at $L_{\text{total}}/M_{\text{core}} = 1.149 L_{\odot}/M_{\odot}$.

The properties of the effective emissivity, the luminosity, and the temperature are described in the following subsections. It is found overall that the dependence of the effective parameters on dust temperature is not strongly affected by

the shape of the filaments. For the same overpressure, the central extinction of a cylinder is indeed lower. However, when averaging over the orientations the different geometry produces in the mean an extinction close to the one of a spherical filament. The dust temperature for a given overpressure is therefore closely the same.

As shown in Sect. 2.1.2 at high overpressure, as for highly embedded cores, the radiative transfer problem does not strongly depend on the external pressure. Therefore, the effect of the external pressure on the parameters of the modified black-body spectrum weakens towards colder dust temperatures from cores.

3.2.1. The effective dust emissivity

In Fig. 9, I present the spectral index β and the emissivity κ_0 at $\lambda_0 = 250 \mu\text{m}$ as functions of the dust temperature of the cores. In all cases, the emissivity is lower than the corresponding mean value. Furthermore, the emissivity is less steep with $\beta < 1.8$ in all cases. The parameters β and κ_0 are lower in higher pressure regions. The origin of the flatter emissivity is discussed in Sect. 4.1.

As the figure shows, the emissivity varies as a function of the dust temperature. This dependence decreases with the external pressure. In the high pressure region, the emissivity for $A_V < 16$ mag shows only a mild dependence on dust temperature with $\beta \approx 1.5$. In lower pressure regions, the emissivity is flatter in colder cores. For the ISM pressure, β decreases from 1.75 to 1.55. For typical GMCs with $A_V = 8$ mag, β is close to 1.6. The flattening reflects the increasing optical depth with extinction A_V through the filaments as shown in Sect. 2.1.2. This dependence is strongest in the lowest pressure region. For highly embedded cores with $A_V > 32$, the apparent emissivity steepens again and seems to approach that corresponding to the intrinsic dust properties. The behavior is discussed in Sect. 4.1.

As can be seen from their functional dependence on dust temperature, the values of β and κ_0 are strongly correlated. A low β is accompanied by a low κ_0 as shown in Fig. 10. This correlation is most apparent for regions with $p_{\text{ext}}/k < 10^6$ K/cm³ and extinction values $A_V < 16$ mag, where the data points exhibit only very small deviations from the fitted polynomial functions.

3.2.2. Luminosity of passively heated cores and the $P - T$ -relation

The model relates the L/M -ratio and the effective dust temperature of the core to the central pressure in the filaments surrounding the core (Fig. 11). For a given shape, *ISRF*, external pressure, and extinction, the ratio is independent of the true size of the core since both the luminosity and the mass, by mean of the mass-radius relation, are proportional to R_{core}^2 .

If the flux heating a non-embedded core is completely absorbed, the luminosity becomes $L = 4\pi R_{\text{core}}^2 \pi J^{\text{ISRF}}$, where J^{ISRF} is the integrated flux of the *ISRF*. Ignoring the emission of the CMB, the *ISRF* provided by Mathis et al. (1982) has an energy density $u = \frac{4\pi}{c} J = 0.46$ eV/cm³. Adopting the mass-radius relation (Eq. 3), the luminosity-mass ratio is given by

$$L/M_{\text{core}} = 1.6 \left(\frac{p_{\text{ext}}/k}{2 \times 10^4 \text{ K/cm}^3} \right)^{-\frac{1}{2}} L_{\odot}/M_{\odot}. \quad (17)$$

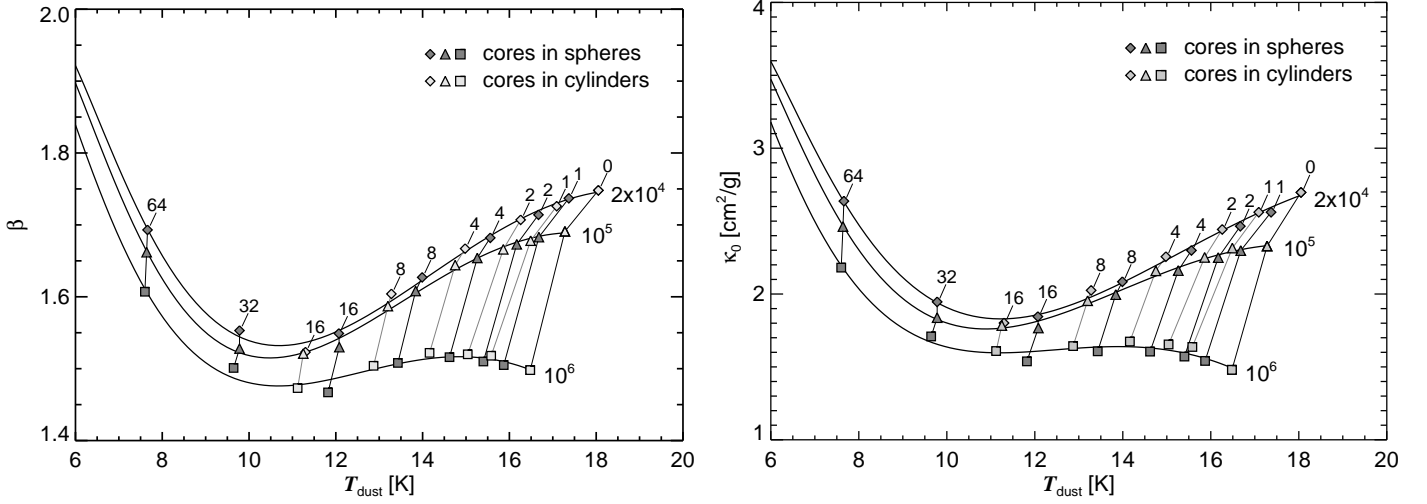


Fig. 9. β and κ_0 as functions of the effective dust temperature T_{dust} for the dust re-emission spectrum for cores assuming diffuse dust. The cores are either embedded in spherical or cylindrical filaments. The external pressure p_{ext}/k outside the filaments is assumed to be 2×10^4 , 10^5 , or 10^6 K/cm³. The corresponding theoretical values labelled by the considered central extinction A_V of the filaments are shown either as diamonds, triangles, or squares. The values obtained for a given external pressure are fitted with a polynomial function shown as solid black lines.

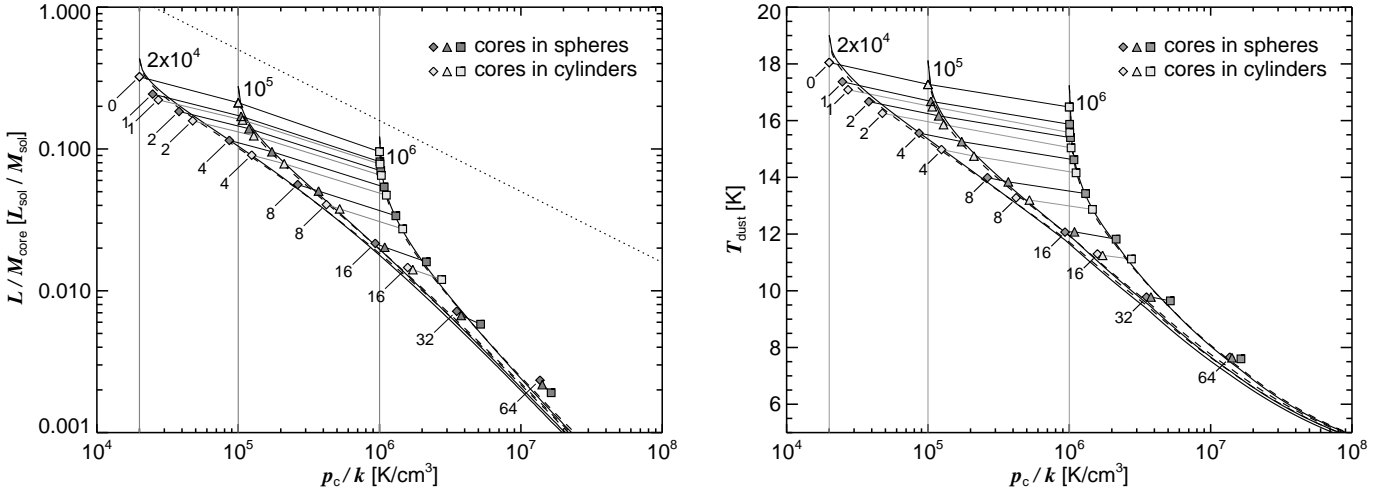


Fig. 11. L/M -ratios (left-hand figure) and the effective dust temperatures (right-hand figure) for embedded passively heated cores. The values obtained using ray-tracing (symbols) are compared with the approximate solutions for cores in spheres (solid curves) and cylinders (dashed curves). The different symbols refer to the external pressures (shown as vertical grey lines) assumed in the calculations: diamonds 2×10^4 K/cm³, triangles 10^5 K/cm³, and squares 10^6 K/cm³. They are labelled according to the extinction A_V through the filament center. The dotted line in the left-hand figure shows the asymptote Eq. 17 for non-embedded cores ($A_V = 0$ mag), where the external radiation heating the core is completely absorbed.

As seen in Fig. 11, the curve provides an upper limit to the true L/M -ratios. For non-embedded cores pressurized by the mean ISM pressure, the ratio is, despite the high extinction through the core center, lower by more than a factor of two, even if the total luminosity of the SED (as given in Table 1) is considered. One reason is the steep density profile of the cores and the consequently strong variation in the optical thickness with the impact parameter of individual rays passing the core. A core that appears opaque in the center can still be optically thin or marginally optically thick at the outskirts, so that only radiation towards the core center will be strongly attenuated. The amount of light absorbed in the core is further reduced by the clouds' albedo.

The overall increase in the extinction with pressure ($A_V \propto \sqrt{p_c}$) leads together with the decrease in the albedo to a stronger absorption in higher pressure regions. The L/M -ratio asymptotically approaches, as shown in Fig. 12, the curve given by Eq. 17.

As shown in Fig. 11, the simplified RT-model reproduces to first order not only the L/M -ratio but also the effective temperatures obtained using the full calculations. The deviations are caused by the absence of the PAH emission in the simplified model, which is accurately accounted for in the full radiative transfer calculations. In the simplified model, all the absorbed UV and optical light is re-emitted in the FIR, which is otherwise re-emitted mostly by PAH molecules in the NIR and MIR. For extinction values below

Table 1. SED Parameters of Embedded Cores ($T_{\text{eff}} = 10$ K)

A_V	p_c/k [$10^4 \frac{\text{K}}{\text{cm}^3}$]	$\sqrt{1/\chi_{\text{red}}^2}$ [%]	T_{dust}^a [K]	β^b	κ_0^c [$\frac{\text{cm}^2}{\text{g}}$]	L^d [L_{\odot}]	L/M_{core} [$\frac{L_{\odot}}{M_{\odot}}$]	L_{total}^e [L_{\odot}]	$L_{\text{total}}/M_{\text{core}}$ [$\frac{L_{\odot}}{M_{\odot}}$]	$FWHM^f$ [R_{cl}]	F_{Gauss}^g [F_{model}]
($p_{\text{ext}} = 2 \times 10^4 \text{ K/cm}^3, \chi = 1$)											
0	2.00	3.05	18.05	1.748	2.697	0.829	0.323	1.081	0.421	1.081	1.077
Cores in the center of spherical clouds											
1	2.48	2.92	17.37	1.737	2.561	0.562	0.244	0.675	0.293	1.059	1.062
2	3.82	2.79	16.67	1.714	2.465	0.343	0.184	0.391	0.210	1.062	1.064
4	8.65	2.83	15.56	1.682	2.299	0.142	0.115	0.152	0.123	1.086	1.073
8	26.36	3.02	13.99	1.627	2.084	3.99(-2)	5.61(-2)	4.09(-2)	5.79(-2)	1.131	1.085
16	93.22	3.51	12.07	1.549	1.845	8.12(-3)	2.16(-2)	8.13(-3)	2.18(-2)	1.176	1.090
32	351.7	3.58	9.78	1.553	1.946	1.37(-3)	7.07(-3)	1.39(-3)	7.19(-3)	1.223	1.101
64	1365.	2.51	7.66	1.693	2.637	2.30(-4)	2.34(-3)	2.35(-4)	2.39(-3)	1.247	1.105
Cores in the center of cylindrical clouds											
1	2.72	2.84	17.09	1.726	2.561	0.489	0.222	0.577	0.262	1.056	1.062
2	4.76	2.78	16.26	1.707	2.443	0.263	0.158	0.293	0.176	1.066	1.066
4	12.46	2.88	14.98	1.667	2.256	9.30(-2)	9.04(-2)	9.30(-2)	9.57(-2)	1.099	1.076
8	42.04	3.18	13.28	1.604	2.025	2.27(-2)	4.05(-2)	2.32(-2)	4.14(-2)	1.151	1.090
16	158.1	3.79	11.30	1.523	1.801	4.22(-2)	1.46(-2)	4.27(-3)	1.48(-2)	1.202	1.098
($p_{\text{ext}} = 1 \times 10^5 \text{ K/cm}^3, \chi = 1$)											
0	10.0	3.06	17.28	1.691	2.329	0.243	0.211	0.3021	0.263	1.151	1.091
Cores in the center of spherical clouds											
1	10.48	2.96	16.68	1.683	2.298	0.191	0.170	0.223	0.199	1.130	1.083
2	11.92	2.92	16.17	1.673	2.250	0.147	0.139	0.164	0.156	1.123	1.082
4	17.33	2.92	15.26	1.654	2.161	8.34(-2)	9.56(-2)	8.90(-2)	0.102	1.128	1.084
8	37.01	3.10	13.84	1.608	1.996	3.02(-2)	5.05(-2)	3.11(-2)	5.20(-2)	1.154	1.090
16	108.7	3.56	12.08	1.530	1.767	7.06(-3)	2.03(-3)	7.14(-3)	2.05(-2)	1.202	1.104
32	378.2	3.64	9.78	1.528	1.838	1.25(-3)	6.70(-3)	1.27(-3)	6.81(-3)	1.233	1.103
64	1417.	2.57	7.64	1.662	2.463	2.10(-4)	2.18(-3)	2.14(-4)	2.22(-3)	1.262	1.110
Cores in the center of cylindrical clouds											
1	10.73	3.00	16.49	1.678	2.315	0.178	0.160	0.203	0.184	1.122	1.081
2	12.89	2.96	15.86	1.666	2.251	0.126	0.124	0.138	0.137	1.118	1.081
4	21.14	2.97	14.75	1.644	2.159	6.22(-2)	7.87(-2)	6.55(-2)	8.30(-2)	1.131	1.085
8	52.21	3.24	13.20	1.587	1.954	1.90(-2)	3.78(-2)	1.94(-2)	3.86(-2)	1.161	1.088
16	171.9	3.82	11.25	1.521	1.784	3.92(-3)	1.41(-3)	3.97(-3)	1.42(-2)	1.208	1.099
($p_{\text{ext}} = 1 \times 10^6 \text{ K/cm}^3, \chi = 1$)											
0	100.0	3.79	16.48	1.498	1.480	3.47(-2)	9.57(-2)	0.0409	0.113	1.311	1.125
Cores in the center of spherical clouds											
1	100.5	3.70	15.87	1.505	1.541	2.94(-2)	8.13(-2)	3.29(-2)	9.09(-2)	1.283	1.111
2	102.0	3.59	15.40	1.510	1.571	2.53(-2)	7.02(-2)	2.74(-2)	7.62(-2)	1.280	1.119
4	107.8	3.47	14.62	1.516	1.605	1.89(-2)	5.39(-2)	1.98(-2)	5.67(-2)	1.256	1.108
8	130.4	3.50	13.43	1.508	1.607	1.08(-2)	3.38(-2)	1.10(-2)	3.47(-2)	1.245	1.105
16	214.4	3.83	11.82	1.467	1.538	3.97(-3)	1.60(-2)	3.99(-3)	1.62(-2)	1.247	1.106
32	518.7	3.54	9.644	1.501	1.709	9.26(-4)	5.81(-3)	9.42(-4)	5.91(-3)	1.278	1.121
64	1638.	2.68	7.60	1.607	2.181	1.71(-4)	1.91(-3)	1.75(-4)	1.95(-3)	1.298	1.123
Cores in the center of cylindrical clouds											
1	100.7	3.68	15.58	1.518	1.637	2.83(-2)	7.83(-2)	3.13(-2)	8.66(-2)	1.279	1.121
2	102.9	3.59	15.04	1.520	1.654	2.33(-2)	6.51(-2)	2.50(-2)	6.98(-2)	1.254	1.107
4	111.7	3.51	14.16	1.522	1.674	1.62(-2)	4.72(-2)	1.69(-2)	4.92(-2)	1.241	1.104
8	145.8	3.61	12.87	1.504	1.643	8.22(-3)	2.73(-2)	8.38(-3)	2.79(-2)	1.238	1.104
16	275.1	4.01	11.12	1.473	1.609	2.62(-3)	1.20(-2)	2.65(-3)	1.20(-2)	1.246	1.105

^(a) Effective dust temperature of the modified black-body fit.

^(b) Power of the effective emissivity $\kappa_{\lambda}^{\text{em}} = \kappa_0(\lambda/\lambda_0)^{-\beta}$ where κ_0 is the effective emissivity at $\lambda_0 = 250 \mu\text{m}$.

^(c) Effective emissivity per dust mass at $\lambda_0 = 250 \mu\text{m}$.

^(d) Luminosity of the modified black-body fit.

^(e) Total luminosity of the dust re-emission.

^(f) $FWHM$ of the Gaussian source approximation of the surface brightness at $250 \mu\text{m}$.

^(g) Flux of the Gaussian source approximation of the surface brightness at $250 \mu\text{m}$.

$A_V = 4$ mag, the heating of the dust grains in the cores is overestimated leading to a higher dust temperature. In the case of highly opaque filaments (above $A_V \sim 8$ mag), the PAH emission of the filaments leads in the full RT calcu-

lation to an increasingly important heating source, which gives rise to the warmer dust temperatures (Sect. A).

The curves for the lowest external pressure provide a lower limit to both the L/M -ratio and the dust temperature of cores. Above the curves, passively heated cores are

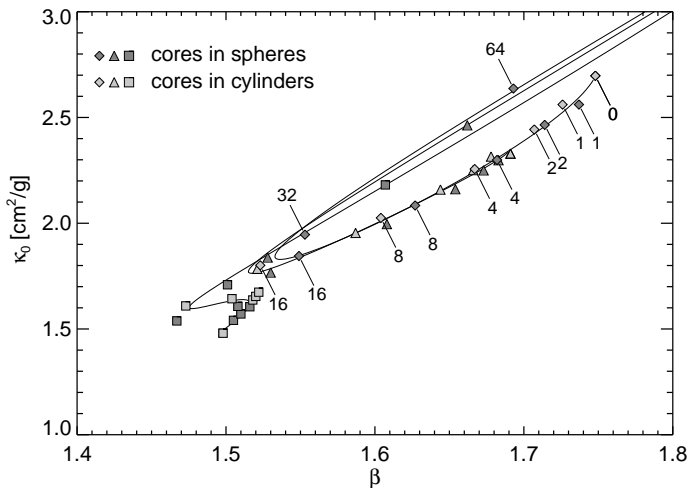


Fig. 10. Relation of the effective values κ_0 and β derived by fitting a modified black-body function to the theoretical dust emission spectrum of condensed cores. The symbols represent the same external pressure p_{ext}/k of the medium surrounding the filaments as in Fig. 9 (diamonds for 2×10^4 K/cm³, triangles for 10^5 K/cm³, and squares for 10^6 K/cm³.) The symbols corresponding to filaments pressurized by the mean ISM pressure are labeled with the assumed central extinction of the filament. The curves are the derived fits for β and κ_0 shown in Fig. 9.

embedded in filaments, which are surrounded by a higher pressure gas. The cores are also located in this region if they are heated by an additional source such as a progenitor star in the core or an additional external source.

The resulting relation between the L/M -ratio and the effective dust temperature T_{dust} for a given external pressure is shown in Fig. 12. For the same L/M -ratio, the dust in embedded cores appears to be warmer in high pressure regions of the ISM because the SED is largely determined by the relative warm dust emission at the outskirts of the cores. The L/M -ratios for low external pressures lie on a curve that is slightly flatter than a simple power law as shown in the figure. The power-law fit provides a constant emissivity with $\beta = 1.96$ and $\kappa_0 = 2.15$ cm²/g.

3.3. Brightness profile

Radiative transfer effects cause the brightness profiles of the dust emission spectrum to be broader than the intrinsic profile of the column density profile (Fischera & Dopita 2008). The profiles of the surface brightness at three far infrared wavelengths, which correspond to the bolometers of the Herschel satellite’s SPIRE-instrument (and of the balloon experiment BLAST), are shown in Fig. 13. The profile steepens towards longer wavelengths. This effect is caused by the emission at longer wavelengths being dominated by larger grains, which have lower radial temperature variations than the smaller dust grains that dominate at shorter wavelengths. In addition, the emission at shorter wavelengths is more affected by temperature variations because these regions are blueward of the Rayleigh-Jeans limit. The steepening of the profile increases for highly embedded cores (as the cores are more optically thick) that are affected by stronger radial temperature variations.

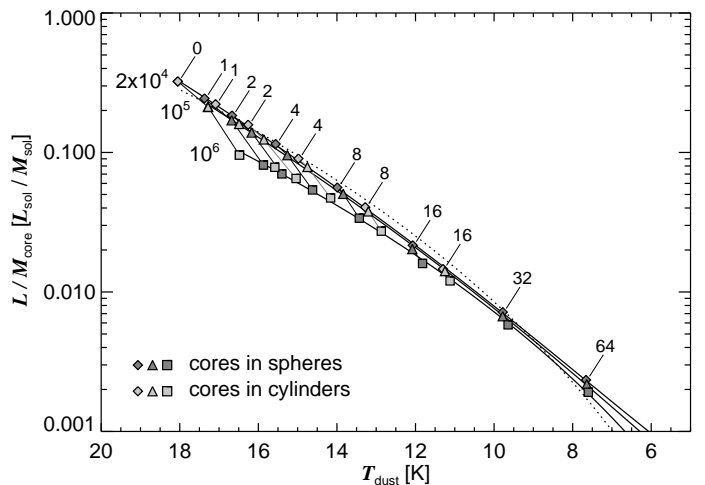


Fig. 12. Light-to-mass ratio (L/M) of the dust luminosity and the core mass as function of the dust temperature of embedded cores. The derived ratios are labelled with the assumed extinction values A_V through the filaments center. The ratios $L/M_{\text{core}}(T_{\text{dust}})$ obtained for cores that are embedded in cylindrical and spherical filaments for each given external pressure p_{ext}/k (2×10^4 , 10^5 , 10^6 K/cm³) are fitted by a polynomial function shown as solid black lines. The points for mean ISM pressure are fitted also by a simple power law (dotted curve).

The cores are often modeled observationally as Gaussian sources (see e.g., Netterfield et al. (2009) and Olmi et al. (2009)). To facilitate comparison of observations to my models, I approximate the surface brightness at $250 \mu\text{m}$ by a two-dimensional Gaussian function. A Gaussian function is broader than the profile of the column density, but as can be seen in Fig. 13, a Gaussian function can be a good representation of the true emission profile as in case of cores embedded in filaments with $A_V < 8$ mag that are confined by the mean ISM pressure. The FWHM of the Gaussian function is a good estimate of the physical radius of the core (Fig. 14) albeit too large by 10%. The Gaussian approximation becomes worse in high pressure regions or for highly embedded cores where the cores are more compact. The error in the size estimate based on the FWHM increases therefore towards lower dust temperatures. The Gaussian approximation for highly embedded cores is too narrow, overestimating the flux passing through the core center and inferring a FWHM considerably larger than the intrinsic core radius (Fig. 14). The estimated flux using a Gaussian approximation is slightly too high (6% to 12% overestimate) depending on the external and internal pressure of the filament. The flux estimate tends to be more accurate in the lower pressure regions of the ISM.

4. Discussion

My model connects the effective dust temperature to the physical properties of passively heated embedded cores. In particular, it establishes a relation between the dust temperature and the pressure of the medium surrounding the cores. The details of the relationship are determined by the ISRF, the dust properties in the cores, and the external pressure confining the filaments but is independent of the actual mass of the cores. This model can be directly tested

Table 2. Polynomial approximations

p_{ext}/k [K/cm ³]	a_0	a_1	a_2	a_3	a_4	a_5
$\beta = \sum_i a_i (\log_{10} T_{\text{dust}} [\text{K}])^i$						
2×10^4	-40.7509	186.611	-296.453	202.709	-50.5764	—
1×10^5	-41.0076	190.600	-307.465	213.560	-54.1691	—
1×10^6	-29.0751	144.608	-243.478	175.672	-46.2471	—
$\kappa_0 [\text{cm}^2/\text{g}] = \sum_i a_i (\log_{10} T_{\text{dust}} [\text{K}])^i$						
2×10^4	-133.777	600.783	-948.039	639.586	-156.646	—
1×10^5	-142.593	654.894	-1060.36	735.858	-185.995	—
1×10^6	-90.8491	461.490	-802.533	592.289	-158.761	—
$\log_{10} L/M_{\text{core}} [L_{\odot}/M_{\odot}] = \sum_i a_i (\log_{10} T_{\text{dust}} [\text{K}])^i$						
2×10^4	-2.63348	-4.06995	4.60187	—	—	—
1×10^5	-3.27281	-2.87834	4.03329	—	—	—
1×10^6	-6.11354	2.87895	1.09179	—	—	—
$FWHM [R_{\text{cl}}] = \sum_i a_i (T_{\text{dust}} [\text{K}])^i$						
2×10^4	1.04042	0.193172	-0.0506557	0.00579236	-0.000312315	6.33987e-06
1×10^5	1.01551	0.198970	-0.0502195	0.00571245	-0.000313287	6.59132e-06
1×10^6	1.29788	-0.0283919	0.0144707	-0.00232888	0.000140731	-2.79548e-06

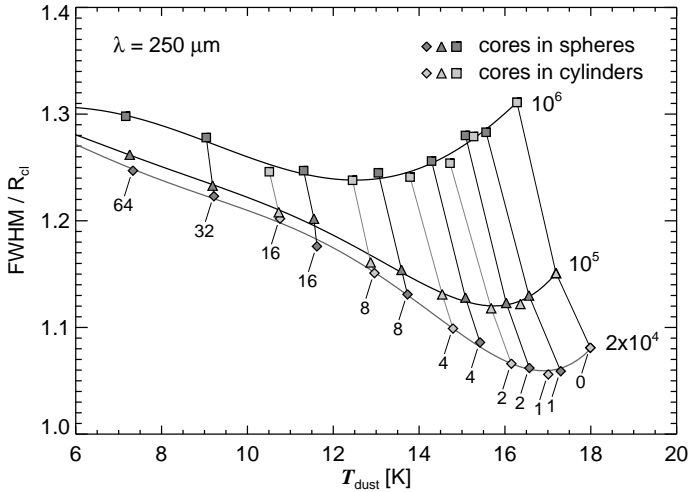


Fig. 14. FWHM at $\lambda = 250 \mu\text{m}$ of a Gaussian representation of the surface brightness profile of cores which are either embedded in spherical or cylindrical filaments. The data points for each assumed external pressure are fitted with a polynomial function shown as solid lines.

by high resolution observations in the FIR/submm regime, which allow apart from measuring the core mass by modeling the dust emission spectrum also a determination of the size of the core and by applying the mass-radius relation (Eq. 3) the pressure around the core.

The model relates essential core parameters such as the $FWHM$, the emissivity (β and κ_0), and the luminosity-mass ratio to the pressure of the medium surrounding the filaments and the extinction through the filaments' center, which corresponds (for a given filament shape) to a certain central pressure. The values of the parameters are found to be (for a given external pressure) controlled mainly by the dust temperature, which allows in principle a simple correction for radiative transfer effects. Future work needs to determine how shapes of the ISRF, the dust properties, and the structure of the molecular clouds caused by the turbulent motion affect the core models, allowing a clearer understanding of the uncertainties associated with the mea-

surement of core masses. The expected basic effects are discussed in Sects. 4.2.1, 4.2.2, and 4.3. A additional complication is caused by the coupling of gas and dust in high density environment, although the effect might be less important if the cores are mainly supported by turbulent motion.

4.1. The origin of the effective dust emissivity

The emissivities of my models differ considerably from the mean properties derived in Sect. 2.2.1. There are two major reasons why the dust emissivity seems to be less steep and also lower. First, the variation in dust temperatures with size and composition at each radial distance in the core and second the smooth variation in the dust temperatures with position in the core.

Even without additional radiative transfer effects the parameters of the emissivity have been shown (Sect. 3.2) deviate from the intrinsic mean values. The reason is that the emission behavior depends on both grain size and grain composition. The mass of the dust grains is contained in the large grains, which are also the coldest with temperatures much below 19 K. The warm dust temperature is caused by the smallest dust grains, which do not contain much mass but efficiently absorb interstellar radiation. As a result their emission dominates the blue side of the SED and, to a large extent, its peak. At larger wavelengths, the overall dust emission is gradually enhanced by the emission of colder and larger grains, which flattens the emission profile. To compensate for the warm dust and the low mass related to the dust emission, the emissivity is reduced to obtain the true dust mass.

A similar effect is caused by the gradually changing dust temperature with radius. The emission from warm dust grains located at large cloud radii dominate the bulk of the SED and determine to a large part the position of the peak of the dust emission and therefore the effective dust temperature. This is most clearly demonstrated by the similar effective temperature shown in Fig. 11 and the dust temperature at the cores' edge as shown in Fig. 5. At longer wavelengths, the integrated dust emission spectrum is grad-

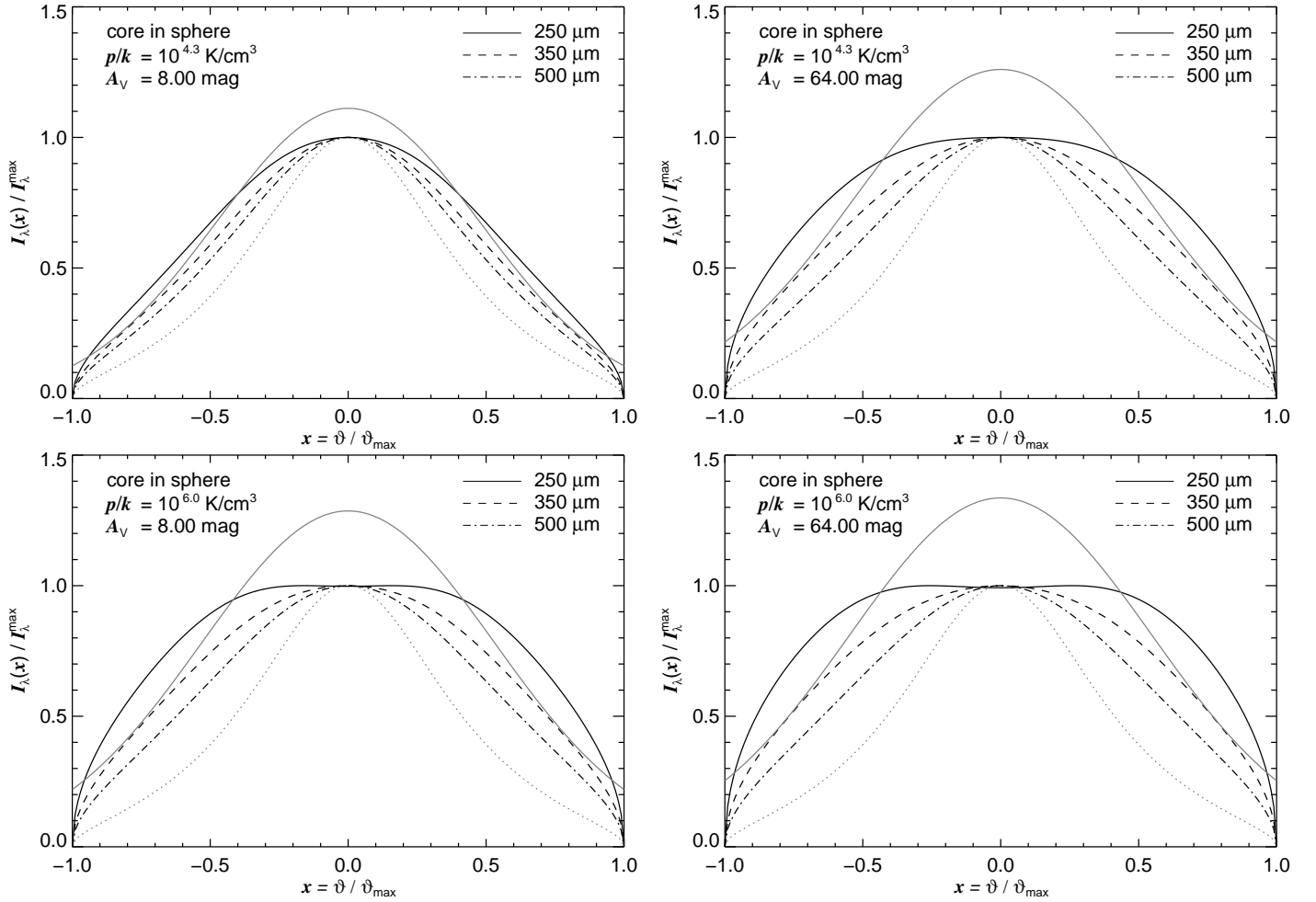


Fig. 13. Brightness profiles at 250, 350, and 500 μm . They are compared with the profile of the column density (dotted line). The surface brightness at 250 μm is fitted to a Gaussian source (grey line). The filaments are either confined by a medium with $p_{\text{ext}}/k = 2 \times 10^4 \text{ K/cm}^3$ (top) or 10^6 K/cm^3 (bottom). The extinction through the filaments' center is either $A_V = 8 \text{ mag}$ or $A_V = 64 \text{ mag}$ (left-hand figure and right-hand figure, respectively).

ually more affected by colder dust grains in the interior of the cloud. The shape of the dust re-emission overall appears to be flatter than expected for the underlying dust emissivity. As the dust emission is dominated by the warm dust grains, the absolute emissivity needs to be reduced to account also for the emission of cold dust grains. As seen, the effect can be larger than a factor of two depending on the radiation field heating the core and how opaque the core actually is.

As seen, the effect of the temperature distribution inside the core on the apparent emissivity increases for a given central extinction of the filaments with external pressure and (for given external pressure $p_{\text{ext}}/k < 10^6 \text{ K/cm}^3$) with extinction of the filaments until the filaments become highly opaque with $A_V > 16 \text{ mag}$. The steepening of the apparent emissivity for embedded cores in filaments with $A_V > 16$ is caused by an overall reduction in the temperature variation inside the core both in terms of the location as seen in Fig. 5 and in terms of grain composition and grain size that occurs for of highly reddened radiation fields. The reason for the latter phenomenon is given in Sect. 3.1.3. The reduced radial temperature variation as seen in Fig. 5 is caused by the additional heating of the grains in the core center by the

dust emission from the filament. A similar effect is expected if the dust emission from the Galactic disc is considered.

A physical limit exists for embedded cores that become predominantly heated by the CMB background radiation. In this situation, the dust in the core approaches the temperature of the CMB independently of the position and composition or size and the apparent emissivity becomes equal to the intrinsic dust emissivity.

The temperature variation is probably also the explanation of the flatter emissivity observed in other astrophysical objects such as galaxies for example (Dunne & Eales 2001; Chakrabarti & McKee 2008). However, in the literature the possibility of a dependence of the emissivity on the dust properties is explored (see discussion by Dunne & Eales (2001)).

4.2. Basic model uncertainties

4.2.1. Uncertainties in the ISRF

The *ISRF* applied in the model is a canonical approach to calculate the dust re-emission from dust grains located in the ISM. However, a large fraction of the radiation in the galactic disc is caused by dust grains and PAH molecules,

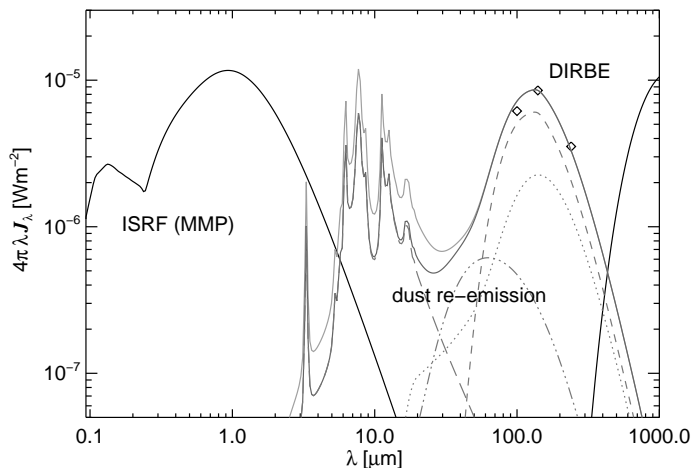


Fig. 15. Mean interstellar radiation field assumed to model the SEDs of embedded cores. The solid black line is the ISRF caused by the stellar light as provided by Mathis et al. (1982). The grey line shows the assumed angle-averaged dust re-emission. The contribution of the PAH emission is reduced relative to the dust re-emission of the diffuse ISM (Fischera, in prep.) shown as light grey curve. The strength of the radiation field is scaled to the DIRBE flux at $140 \mu\text{m}$. The DIRBE fluxes at 100 , 140 , and $240 \mu\text{m}$ are shown as open diamonds. The dust emission is divided into its several components: PAH (long dashed line), graphite (short dashed line), silicates (dotted line), and iron (dashed-dotted line).

which efficiently absorb the light in the UV and optical light. For comparison with the results presented in this paper, I considered an *ISRF* where the dust re-emission from the Galaxy is taken into account. The most important contribution arises from the PAH emission and possibly small stochastically heated grains. In general, this problem needs to be addressed more quantitatively based on all sky surveys such as the DIRBE experiment. The determination of the corresponding mean intensity inside the Galaxy is complicated by the spectral range being dominated by the zodiacal light. The approach presented here is qualitative, but demonstrates where the heating by dust grains and PAH molecules becomes important.

The mean intensity of the dust emission consists primarily of three components: emission from the diffuse gas, HII-regions, and dense clouds (which potentially contain a large percentage of the interstellar material considering that probably up to 30% of hydrogen is molecular (Ferrière 2001)). One of the main differences between the three components is the strength of the PAH emission. In dense clouds, it is likely that the PAH molecules are condensed onto grains. If present, the PAH molecules would be heated by highly attenuated optical and UV radiation, which would reduce considerably the PAH emission relative to the dust emission peak. Additional PAH emission and warm dust emission (around 60 K) arises from HII-regions. I assume that the average PAH emission is lower than the PAH emission from the diffuse phase by a factor of 2. Otherwise the dust re-emission is assumed to be the same as in the diffuse ISM. I use the same dust properties as in the ray-tracing calculations. The SED of the dust emission is derived assuming a non-attenuated *ISRF*. The strength of the dust emission is obtained by scaling

the emission at $140 \mu\text{m}$ to the corresponding mean intensity of the DIRBE experiment ($\nu J_\nu = 6.78 \times 10^{-7} \text{ W/m}^2$). The assumed total SED of the mean *ISRF* is displayed in Fig. 15. I derived the DIRBE fluxes shown in the figure using all sky DIRBE data from which the zodiacal light had been subtracted using a physical model. The colder dust emission from compact clouds relative to the emission from diffuse dust grains has only a small effect on the heating of the cores and is ignored. I also neglect the warm dust component from HII-regions. In this model (Fig. 15), 34% of the Galactic mean intensity in the solar neighborhood is caused by dust grains and PAH molecules.

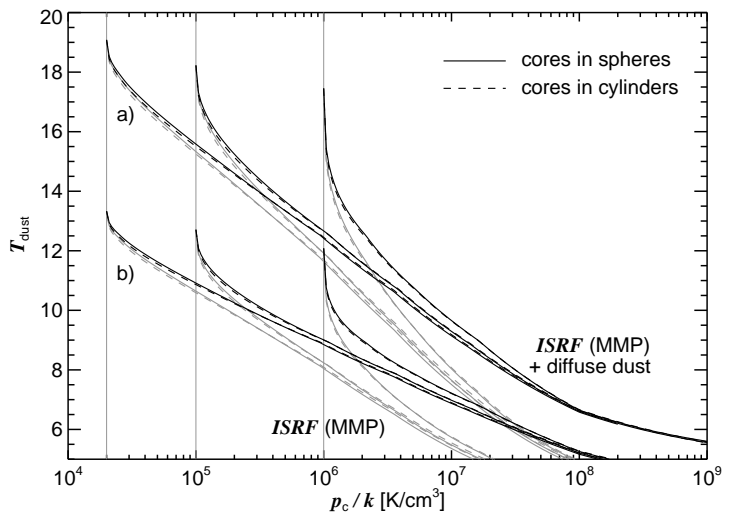


Fig. 16. Effective temperatures of embedded cores as a function of the central pressure in the filament, which is assumed to be either a self-gravitating sphere or a self-gravitating cylinder. In case *a*), the emissivity is assumed to be the same as in the diffuse dust model, while in *b*) the emissivity is increased by a factor 8. The external pressure outside of the filaments is assumed to be 2×10^4 , 10^5 , and 10^6 K/cm^3 . The filaments are heated either by the *ISRF* as provided by Mathis et al. (1982) (grey lines) or by an *ISRF* where the diffuse dust emission is added.

In Fig. 15, the PAH emission of the assumed *ISRF* is clearly stronger (despite it being fainter than the diffuse dust emission) than the PAH emission at the center of the filaments (Fig. 3). This implies that, even if PAH emission arises from the filaments, it is less important for heating the dust in the core than the Galactic IR emission. The result for the modified *ISRF* is shown in Fig. 16. The additional heating by IR photons becomes important only for highly embedded cores where the central extinction of the filaments is larger than $A_V \sim 8 \text{ mag}$. This additional heating is more important for the inner core regions, which lead to a steeper brightness profile.

4.2.2. Uncertainties in the emissivity

The results presented in this paper depend to a certain degree on the dust model, which determines both the position of the peak of the dust re-emission spectrum and its shape. A different dust model will therefore lead to different effective dust parameters being assigned to the derived dust emission spectra for embedded cores. This will also be true

if the results are compared with calculations based on the dust model of Weingartner & Draine (2001), which has a different assumed dust composition and size distribution. However, since both models were constructed to reproduce the observed properties in the diffuse ISM the differences should be small relative to the large uncertainties in the dust properties of the dense phase.

The calculations are based on the dust properties of the diffuse medium merely as a reference point. Grains in the dense phase are likely to form icy layers that will, as a consequence, increase the sticking coefficient and therefore accelerate the grain growth process by means of grain coagulation (see discussion in Fischera & Dopita (2008)). The process will naturally alter the size distribution of the grains by removing the number of small grains while increasing the mass of the largest dust particles. This will result in a rather flat slope of the extinction curve in the UV, which is generally determined by the abundance of small grains. Its effect on the optical properties in the far infrared is uncertain but the emissivity may be considerably higher. According to Kruegel & Siebenmorgen (1994), a factor of 10 higher emissivity is physically possible depending on the properties of the composites. In addition, the grain growth models presented by Ossenkopf & Henning (1994) depend on the density inside the clouds. If correct, a higher emissivity is expected in denser clouds. The mass estimate of cores is observationally based on an emissivity at $250 \mu\text{m}$ of $\kappa_0 = 10 \text{ cm}^2/\text{g}$ (Netterfield et al. 2009; Olmi et al. 2009) with $\beta = 2$ and a gas-to-dust mass-ratio of 100. Despite this relatively low gas-to-dust mass ratio, the cores appear to be far less massive than they would be if the masses were based on the emissivities derived in this paper.

Figure 16 shows a first-order effect of a higher emissivity on the core temperature. It is assumed that the spectral index β has the same dependence on the pressure. In this case, the core temperature varies as $T_{\text{dust}}^{(2)} = T_{\text{dust}}^{(1)} (\kappa_{0,1}/\kappa_{0,2})^{1/(4+\beta)}$. In the special case where the emissivity of the dust grains has increased by a factor 8, the absorption coefficient above $60 \mu\text{m}$ is scaled by the same factor. Between $20 \mu\text{m}$ and $60 \mu\text{m}$, a smooth transition is made. The pressure p_c in the filaments obtained by measuring the mass by modeling the SED and the size of the core varies as $p_c^{(2)} = p_c^{(1)} (\kappa_{0,1}/\kappa_{0,2})^2$ and therefore depends strongly on the emissivity. Too low emissivities will produce too high pressure values. The uncertainty in the emissivity affects observationally only the mass estimate and the pressure. The $P - T$ -relation might therefore be helpful to estimate the dust emissivity in cores.

A first-order correction to the dependence of β , κ_0 , L/M_{core} , and $FWHM$ on T_{dust} is given by replacing the dust temperature with $T_{\text{dust}}^{(2)}$. For the emissivities κ_0 , the values have to be corrected by the corresponding factor. However, the dependence on dust temperature needs to be analyzed quantitatively using more realistic assumptions about the dust properties inside the clouds.

4.3. Effect caused by the inhomogeneous medium

As mentioned in the introduction, molecular clouds are turbulent, which produces a strong variation in the local density and as a consequence a variation in the column density seen through the molecular clouds (e.g. Kauffmann et al. (2010)). The effect of turbulence was studied in some de-

tail by Fischera & Dopita (2004, 2005) and discussed also by Fischera & Dopita (2008), where a method is described that considers how the turbulent density structure in radiative transfer studies through self-gravitating clouds can be taken into account. Fischera & Dopita (2005) illustrated how the dust attenuation can be directly related to the physical condition of the turbulent medium. A statistical treatment of the radiative transfer through the clouds showing a smoothly varying density fluctuations as expected in turbulent clouds was presented by Hegmann & Kegel (2003).

Despite a number of studies about the effect of an inhomogeneous medium on the radiative transfer (Boisse 1990; Witt & Gordon 1996; Wolf et al. 1998; Városi & Dwek 1999; Witt & Gordon 2000; Gordon et al. 2001; Hegmann & Kegel 2003; Doty et al. 2005), the importance for the interpretation of infrared observations is still uncertain. Although similar in nature, not all studies can be directly applied to the problem of externally heated molecular clouds. The problem generally addressed in studies about the radiative transfer through molecular clouds is the effect of the density structure on the dust scattering and dust absorption without considering the dust re-emission (Boisse 1990; Witt & Gordon 1996; Wolf et al. 1998; Witt & Gordon 2000; Hegmann & Kegel 2003). While it is one of the main complications of radiative transfer calculations, Doty et al. (2005) stated (based on test calculations) that dust scattering plays only a very small role in the distributions of dust temperatures in the majority of their sources. They indeed ignored this problem altogether in their study of dust temperatures in molecular clouds.

Because of the complexity of the problem, the model calculations have in most cases been based on rather simplified assumptions about the medium. In general, a two-phase model is considered where randomly distributed dense ‘clumps’ are embedded in an otherwise homogeneous thin medium (Boisse 1990; Witt & Gordon 1996; Wolf et al. 1998; Witt & Gordon 2000; Gordon et al. 2001; Doty et al. 2005). The inhomogeneous medium is typically described by the filling factor of the ‘clumps’, their size relative to the extension of the whole cloud, the density ratio of the ‘clumps’ and the ‘inter-clump’ medium, and in addition by the optical depth of the cloud. The application to observations is complicated by neither the medium as a whole nor the individual clumps being described as physical entities with realistic density profiles.

To some extent, the models of individual dense ‘clumps’ are comparable to the dense self-gravitating cores in my model of embedded cores. From a physical standpoint, it seems, however, more realistic that they form in the inner center of the filaments where they experience the highest pressure rather than to place them randomly inside the filament. Because of the pressure profile, it is also expected that cores located closer to the cloud edges are less optically thick than at the center. My model is less applicable to cores formed in a dense cluster where shadow effects by individual cluster members become important. Although this situation is often considered in two phase models by applying a high filling factor of the ‘clumps’, it becomes observationally difficult to separate the individual sources.

The most important characteristic caused by inhomogeneities is that a non-homogenous dusty medium is more transparent than an inhomogeneous medium

(Boisse 1990; Hegmann & Kegel 2003; Doty et al. 2005; Fischera et al. 2003; Fischera & Dopita 2005). The effect disappears when the density enhancements become optically thin. For typical molecular clouds ($A_V \sim 8$ mag), the increase in transparency is highest in the UV and optical and is negligible in the infrared. The effect leads therefore for a homogeneous extended source seen through a turbulent screen to a flattening of the attenuation curve (Fischera & Dopita 2005). This flattening is characterized by a large absolute-to-relative extinction, the R_V -value being defined as $A_V/(A_B - A_V)$, which is close to 3.1 in the diffuse ISM. The same effect is expected for the turbulent interstellar medium and Fischera et al. (2003) demonstrated that the turbulence can naturally explain the flatter curvature of the Calzetti extinction curve derived for local starburst galaxies. Because of the inhomogeneities, the light most responsible for heating the gas and the dust can therefore penetrate deeper into the filaments and consequently into the core. On the other hand, the total light absorbed inside the core is lower leading effectively to a lower dust temperature, solely by considering the energy balance in the core.

In the framework of the model, the SEDs of the cores are independent of the effective temperature, which determines for a given pressure the mass and the size of the cores inside the filaments. If the cores are supported predominantly by turbulent pressure, more massive cores are also more turbulent, which creates a stronger variation in the local density around the mean. Their one-point statistic of the local density is described by a broader probability distribution approximately described by a log-normal function. It is therefore expected that in a certain pressure region of a GMC, the effect of the turbulent density structure is stronger for more massive cores than for less massive ones.

5. Summary and conclusions

I have presented a physical model for the dust emission of condensed cores where the cores are described by critical stable self-gravitating clouds embedded at the center of self-gravitating filaments. The filaments are assumed to be either spherical or cylindrical in shape. For a set of dust properties and an external isotropic radiation field, the radiative transfer problem is determined by the external pressure confining the filaments and the extinction of the filaments. In the model, the extinction of either a sphere or a cylinder is directly related to the overpressure in the filament center and the external pressure.

The problem has been solved using a ray-tracing technique where the effects of multiple scattering events and the anisotropy of the scattered light are accurately taken into account. The dust emission is derived using a physical dust model of stochastically heated grains of different sizes and compositions. The work focuses on the radiative transfer effects and is therefore based on the dust properties of diffuse dust grains. The mean extinction at FIR wavelengths is approximately described by a simple power law with $\beta^{\text{ext}} = 2.024$ and an absolute extinction at $\lambda_0 = 250 \mu\text{m}$ of $\kappa^{\text{ext}}(\lambda_0) = 5.232 \text{ cm}^2/\text{g}$.

The variation in the dust temperatures inside embedded cores is found to depend on the external pressure and the extinction of the filaments. The variation is not necessarily smaller than for non-embedded cores as stated by Stamatellos & Whitworth (2003).

For comparison with observations, the bulk of the dust re-emission is approximated by a modified black-body spectrum using β and κ_0 of the emissivity $\kappa_\lambda^{\text{em}} = \kappa_0(\lambda/\lambda_0)^{-\beta}$ for $\lambda_0 = 250 \mu\text{m}$ and the dust temperature T_{dust} as free parameters. As shown, the effective parameters of the emissivity can be applied using a single-zone model for the cores. This simplified model reproduces, to first order, the dust temperature of the cores. On the basis of the model assumptions of self-gravitating clouds, the dust temperature of passively heated cores is independent of the mass of the cores. It is found that:

- The effective emissivity κ_0 is considerably lower than the intrinsic extinction. For filament extinction $A_V < 16$ mag, the values of κ_0 are typically a factor 2 to 3 lower than expected using the mean dust properties in the cloud.
- The emissivity is flatter with $\beta < 1.8$. For the mean value of ISM pressure and $A_V < 16$, I found that $1.52 < \beta < 1.74$.
- The effect on κ_0 and β for a given dust temperature increases with external pressure.
- In highly embedded cores with $A_V > 16$, the emissivity becomes equal to the mean extinction value.

The derived surface brightness is considerably broader than the underlying profile of column density, the effect being most prominent at shorter wavelengths. The brightness profiles become flatter for both more embedded cores and higher pressures of the external medium. The surface brightness at $250 \mu\text{m}$ has been compared with a Gaussian source approximation. The agreement is good for less embedded cores, but is poor for strongly embedded cores, where the Gaussian profile is steeper than the model. It is found that:

- The Gaussian source approximation overestimates the total flux by $\sim 10\%$.
- In high pressure regions and highly embedded cores, the $FWHM$ of the Gaussian source approximation overestimates the size of the core by between 10% and 30%.

For direct comparison with observations I have derived, for different ISM pressures, polynomial expressions of the model relations for $\beta(T_{\text{dust}})$, $\kappa_0(T_{\text{dust}})$, $L/M_{\text{core}}(T_{\text{dust}})$, and $FWHM(T_{\text{dust}})$ at $\lambda = 250 \mu\text{m}$. The relations are found to be only mildly affected by the geometry of the filaments. For highly embedded cores, the work indicates that the dust emission from the Galactic disc needs to be considered to model accurately the SED and surface brightness profiles of the cores.

Acknowledgements. The author likes to thank in particular Prof. Brian Schmidt for his overly great support and his encouragement. I further like to thank namely Dr. R. Tuffs and Prof. Peter Martin for their support. I like further thank CITA where I made most of the numerous radiative transfer calculations presented in this paper.

Appendix A: Approximate solution for the dust temperature in cores

In a single temperature model used by observers to interpret their observations and in this paper, the individual dust grains are, independently of their location inside the core, heated by the same mean intensity J_λ^{heat} . In the framework of the model, this intensity is produced by the radiation field at the center of the filament and by the emission

from the dust grains in the core. That the dust temperature does not strongly depend on the heating flux (it varies as the sixth root of the heating rate) allows approximations that I outline in the following. The aim of the model is to provide an equivalent to the time-consuming ray-tracing technique. To be widely applicable, the effects caused by scattering and re-heating by dust grains are taken into consideration. As in case of the more accurate approach using ray-tracing, the solution is derived in two independent consecutive steps by estimating first the mean intensity $J_\lambda(0)$ in the center of the filament and secondly the dust temperature inside the core.

To obtain a most accurate estimate of the attenuated flux caused by the self-gravitating cores and filaments hence a more reliable estimate of the absorbed energy inside the clouds, I still consider clouds with physical density profiles rather than homogeneous clouds. The difference between the important optical properties (their attenuation and escape probability) for the two assumptions about the density distribution inside the clouds is discussed in Sect. B.1 and B.2, where it is shown that an assumption of a homogeneous cloud will lead to an over-estimate of the absorbed flux.

In both steps, the dust temperature in the corresponding cloud is derived. To consider the radiative transfer effects caused by the emission from dust grains, it is assumed that the emissivity $\eta_\lambda^{\text{dust}} = k_\lambda^{\text{em}} B_\lambda(T_{\text{dust}})$ in both the filament and the core is proportional to the hydrogen density n_{H} .

There are in general three different contributions to the intensity $J_\lambda(0)$ at the center of the filament heating the core: (1) the attenuated radiation of the interstellar radiation field illuminating externally the filament, (2) the radiation of the scattered emission, and (3) the dust emission. To derive accurately the last two contributions, a proper radiative transfer treatment is needed.

The light scattered away from the initial direction is partly compensated for by radiation from other initial directions scattered into it. This leads effectively to a lower extinction towards the cloud center. The approximation where the light is scattered in either a forward or backward direction and where the corresponding fraction is determined by the g-factor, the angle-averaged cosine of the scattered intensity, leads to a lower extinction

$$\bar{k}_\lambda^{\text{ext}} = k_\lambda^{\text{ext}} \left(1 - \frac{1}{2} \omega_\lambda (1 + g_\lambda) \right) \quad (\text{A.1})$$

where $\omega_\lambda = k_\lambda^{\text{sca}}/k_\lambda^{\text{ext}}$ is the dust albedo. In the UV and optical, the light is strongly scattered in the forward direction with $g_\lambda > 0.5$ and $\omega_\lambda > 0.5$. This causes the extinction at these wavelengths to be considerably lower than nominal values. The assumption for scattered light has overall less effect for highly embedded cores where the contribution of the scattered emission to the mean intensity inside the filament is weaker.

The dust grains that provide most of the intensity at the center of an optical thick filament are located at the edge of the filament where the dust temperatures are the warmest. Further inside, the grains are heated by a strongly attenuated radiation field, which shifts the dust emission spectrum to longer wavelengths, where the absorption is also weaker. A conservative lower limit to the dust heating is provided by assuming that all the dust emission arises

from a thin shell at the outer surface of the cloud. This provides

$$J_\lambda^{\text{dust}}(0) = \frac{1}{3} (\eta_\lambda^{\text{dust}}/n_{\text{H}}) \frac{1}{2} \langle N_{\text{H}} \rangle(0) e^{-\tau_\lambda^{\text{ext}}(R_{\text{cl}})} \quad (\text{A.2})$$

for a sphere and

$$J_\lambda^{\text{dust}}(0) = \frac{1}{2} (\eta_\lambda^{\text{dust}}/n_{\text{H}}) \frac{1}{2} \langle N_{\text{H}} \rangle(0) \langle e^{-\tau_\lambda^{\text{ext}}} \rangle \quad (\text{A.3})$$

for a cylinder, where $\langle N_{\text{H}} \rangle(0)$ is the corresponding column density of hydrogen at the center of the homogeneous cloud (Fig. B.1). The mean attenuation is given by

$$\langle e^{-\tau_\lambda^{\text{ext}}} \rangle = \int_0^{\pi/2} d\vartheta \sin \vartheta e^{-\tau_\lambda^{\text{ext}}(R_{\text{cl}})/\sin \vartheta}, \quad (\text{A.4})$$

where the optical depth is given by

$$\tau_\lambda^{\text{ext}} = \int_0^{R_{\text{cl}}} (\bar{k}_\lambda^{\text{ext}}/n_{\text{H}}) n_{\text{H}}(r) dr. \quad (\text{A.5})$$

The dust emission of the filament and the core are calculated using energy conservation between the absorbed and the emitted flux. The absorbed luminosity in the cloud caused by the external radiation is given by

$$L_\lambda^{\text{abs,a}} = S_{\text{cl}} \pi J_\lambda (1 - \exp\{-\tau_\lambda^{\text{eff}}(\hat{p}, \tau_\lambda)\}) (1 - \omega_\lambda^{\text{cl}}(\hat{p}, \tau_\lambda)), \quad (\text{A.6})$$

where S_{cl} is the cloud surface, $\tau_\lambda^{\text{eff}}$ the effective optical depth (see B.1), and $\omega_\lambda^{\text{cl}}$ the albedo of the cloud (see B.3). The attenuation and the cloud albedo depend (apart from the shape) on the overpressure $\hat{p} = p_{\text{c}}/p_{\text{ext}}$ and the radial extinction τ_λ . The additional dependence on the non-isotropy of the scattered light is ignored. The luminosity of the dust emission absorbed inside the cloud is obtained using the escape probability, p_{esc} (see B.2),

$$L_\lambda^{\text{abs,b}} = L_\lambda^{\text{dust}} (1 - p_{\text{esc}}(\hat{p}, \tau_\lambda)) (1 - \omega_\lambda^{\text{cl}}(\hat{p}, \tau_\lambda)), \quad (\text{A.7})$$

where $L_\lambda^{\text{dust}} = V_{\text{cl}} \langle n_{\text{H}} \rangle 4\pi \eta_\lambda^{\text{dust}}/n_{\text{H}}$, V_{cl} is the cloud volume, and $\langle n_{\text{H}} \rangle$ the mean hydrogen density. The absorbed luminosity is, on the other hand, equal to

$$L_\lambda^{\text{abs}} = V_{\text{cl}} \langle n_{\text{H}} \rangle (k_\lambda^{\text{abs}}/n_{\text{H}}) 4\pi J_\lambda^{\text{heat}}. \quad (\text{A.8})$$

The external radiation field is therefore reduced to

$$J_\lambda^{\text{heat,a}} = f_\lambda(\hat{p}, \tau_\lambda) J_\lambda, \quad (\text{A.9})$$

where

$$f_\lambda(\hat{p}, \tau_\lambda) = \frac{(1 - \exp\{\tau_\lambda^{\text{eff}}(\hat{p}, \tau_\lambda)\})}{\langle \tau_\lambda \rangle} \frac{1 - \omega_\lambda^{\text{cl}}(\hat{p}, \tau_\lambda)}{1 - \omega_\lambda} \quad (\text{A.10})$$

with the mean extinction of the cloud defined as $\langle \tau_\lambda \rangle = 4V_{\text{cl}}/S_{\text{cl}} \langle n_{\text{H}} \rangle k_\lambda^{\text{abs}}/n_{\text{H}}$. The intensity produced by the dust grains emission is given by

$$J_\lambda^{\text{heat,b}} = \eta_\lambda^{\text{dust}}/k_\lambda^{\text{abs}} (1 - p_{\text{esc}}(\hat{p}, \tau_\lambda)) (1 - \omega_\lambda^{\text{cl}}(\hat{p}, \tau_\lambda)). \quad (\text{A.11})$$

The contribution of the thermal dust emission to the total heating rate from dust grains located in the cloud is derived in an iterative manner.

The contribution of the different components of the radiation considered in the approximation to the total heating rate are shown in Fig. A.1 for cores embedded in spherical filaments, which are pressurized by a medium with

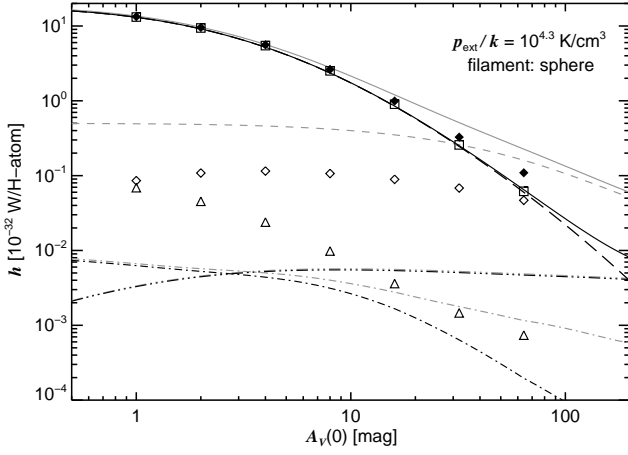


Fig. A.1. Heating rates of the approximation for cores embedded in spherical filaments, given as function of the extinction $A_V(0)$ through the filament center. The assumed external pressure is $p_{\text{ext}}/k = 2 \times 10^4 \text{ K/cm}^3$. The heating rates correspond to the considered *ISRFs* without (black curves) and with dust emission from the ISM (grey lines). The heating rates obtained for an *ISRF* without dust emission from the Galactic disc are compared with the accurate ray-tracing calculation (symbols). The total heating rates (solid lines, filled diamonds) are separated into the several components of the radiation: attenuated external radiation field, which includes the heating by scattered radiation (long dashed lines, open squares); heating by dust emission from the filaments (dashed-three dotted curves, open diamonds); heating by dust emission from the cores (dashed-single dotted curves, open triangles); and dust emission from the Galactic disc (short dashed curve).

$p_{\text{ext}}/k = 2 \times 10^4 \text{ K/cm}^3$. As shown, the simplification for the scattered radiation (Eq. A.1) leads to highly accurate heating rates of the scattered light inside the core. The heating by the dust emission from the filament and the core is considerably lower in this approximation because of the absence of PAH emission. The difference is more prominent for the dust heating from the filaments, also because the approximation provides only a lower limit. Overall the heating by self-absorption inside the cores plays only a minor role in the total heating rate. The heating caused by the dust emission from the filaments provides a more important contribution, which gradually increases with extinction A_V . On the basis of the ray-tracing calculation, this contribution at $A_V = 64 \text{ mag}$ is approximately half of the total heating rate. However, as the figure suggests, for highly embedded cores the dust emission of the galactic disc, in particular the emission from PAH molecules, possibly becomes the predominant heating source.

The effective temperature of the dust emission spectrum is obtained in a procedure often used in radiative transfer problems where it is assumed that grains at a certain location inside the cloud all have the same temperature. The basic difference here is the replacement of the dust emissivity by its effective value to obtain the correct dust temperature in cores. For the filaments, the intrinsic dust emissivity is used. The equations are given here for completeness. The effective temperature is determined by the equilibrium of

the heating and cooling rates

$$\begin{aligned} L^{\text{heat}} &= M_{\text{dust}} \int d\lambda \kappa_{\lambda}^{\text{abs}} 4\pi J_{\lambda}^{\text{heat}} \\ &= M_{\text{dust}} \int d\lambda \kappa_{\lambda}^{\text{em}} 4\pi B_{\lambda}(T_{\text{dust}}) = L^{\text{dust}}. \end{aligned} \quad (\text{A.12})$$

The cooling rate can be written as

$$L^{\text{dust}} = M_{\text{dust}} 4\sigma_{\text{SB}} \langle \kappa^{\text{em}}(T_{\text{dust}}) \rangle T_{\text{dust}}^4, \quad (\text{A.13})$$

where σ_{SB} is the Stefan-Boltzmann constant. The Planck average emission coefficient is given, for a power law ($\kappa_{\lambda}^{\text{em}} = \kappa_0(\lambda/\lambda_0)^{-\beta}$), by

$$\langle \kappa^{\text{em}}(T_{\text{dust}}) \rangle = \frac{\kappa_0}{\lambda_0^{-\beta}} \frac{\Gamma(4+\beta)\zeta(4+\beta)}{\Gamma(4)\zeta(4)} \left(\frac{kT_{\text{dust}}}{hc} \right)^{\beta} \quad (\text{A.14})$$

where k , h , and c are the Boltzmann constant, the Planck constant, and the velocity of light in the vacuum and where $\Gamma(x)$ and $\zeta(x)$ are the Γ -function and the ζ -function.

Appendix B: Effective dust properties of the clouds

In the approximation of the radiative transfer, the absorbed flux inside the core or the filament is derived using an effective value of the dust extinction and an albedo that is based on escape probabilities. To obtain a more accurate estimate of the dust temperature, the values are consistently based on the physical density profile of the clouds rather than assuming that the dusty medium is homogeneously distributed within the given cloud volume. The column density related to the corresponding homogeneous sphere and cylinder is given in Fig. B.1. In the limit of high overpressure $\hat{p} = p_c/p_{\text{ext}}$, the mean column densities through spheres and cylinders are given approximately by

$$\begin{aligned} \langle N_{\text{H}} \rangle(0) &\sim \sqrt{\frac{p_{\text{ext}}/k}{2 \times 10^4 \text{ K/cm}^3}} \\ &\times \begin{cases} 6.50 \times 10^{21} \hat{p}^0 \text{ cm}^{-2} & (\text{sphere}), \\ 4.33 \times 10^{21} \hat{p}^{1/4} \text{ cm}^{-2} & (\text{cylinder}). \end{cases} \end{aligned} \quad (\text{B.1})$$

B.1. Attenuation

The total attenuation described in terms of an effective optical depth caused by the cloud is given by the ratio of the flux density entering the cloud from outside by an isotropic radiation field to the flux density leaving the cloud without being scattered and absorbed. The effective optical depth is therefore given by

$$\tau_{\lambda}^{\text{eff}} = -\ln \left\{ \frac{F_{\lambda}^{-}}{F_{\lambda}^{+}} \right\} = -\ln \left\{ \frac{1}{\pi} \int d\Omega \mathbf{n}_F \cdot \mathbf{n}_J(\Omega) e^{-\tau_{\lambda}(\Omega)} \right\}, \quad (\text{B.2})$$

where \mathbf{n}_F is the normal vector to the surface element the flux density is derived for, \mathbf{n}_J is the vector of the photons illuminating the surface element, and $\tau_{\lambda}(\Omega)$ the total optical depth in direction Ω . For a self-gravitating cloud, the attenuation depends (apart from the actual shape) on the density profile determined by the overpressure $\hat{p} = p_c/p_{\text{ext}}$

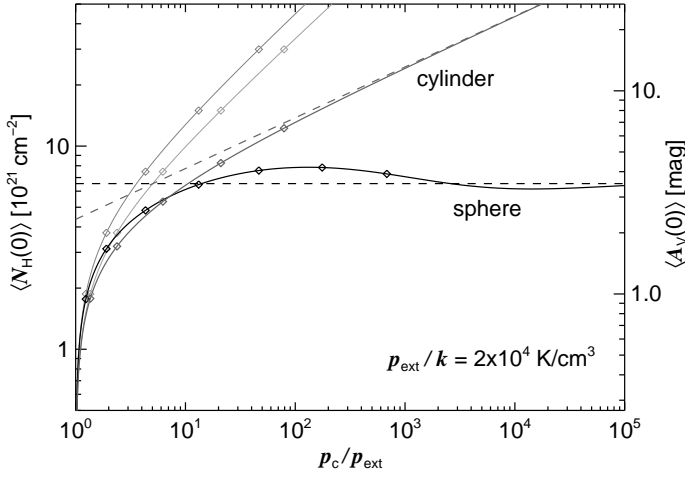


Fig. B.1. Column density at the center of a self-gravitating sphere or a cylinder as a function of the over pressure $\hat{p} = p_c/p_{\text{ext}}$, where the mass is homogeneously distributed within the cloud radius. The column density and the extinction are given for an external pressure $p_{\text{ext}} = 2 \times 10^4 \text{ K/cm}^3$. The asymptotic behavior is shown as dashed lines. The symbols mark the positions of the accurate radiative transfer calculations. For comparison also the true column densities at the cloud centers is shown (light grey curves).

and the radial optical depth τ_λ . For the sphere, the effective optical depth is

$$\tau_\lambda^{\text{eff}}(\hat{p}, \tau_\lambda) = -\ln \left\{ 2 \int_0^{\pi/2} d\vartheta \sin \vartheta \cos \vartheta e^{-\tau_\lambda(\sin \vartheta)} \right\} \quad (\text{B.3})$$

and for the cylinder

$$\tau_\lambda^{\text{eff}}(\hat{p}, \tau_\lambda) = -\ln \left\{ 2 \int_0^{\pi/2} d\vartheta \sin \vartheta \times \int_0^{\pi/2} d\varphi \sin \vartheta \cos \varphi e^{-\tau_\lambda(\sin \varphi)/\sin(\vartheta)} \right\}, \quad (\text{B.4})$$

where the optical depth in the exponent is given by

$$\tau_\lambda(\sin \varphi) = R_{\text{cl}} k_\lambda^{\text{ext}}/n_{\text{H}} \int_{-\cos \varphi}^{\cos \varphi} dl n_{\text{H}} \left(R_{\text{cl}} \sqrt{l^2 + \sin^2 \varphi} \right). \quad (\text{B.5})$$

Since for self-gravitating clouds, $R_{\text{cl}} \propto T/\sqrt{p_{\text{ext}}}$ and $n_{\text{H}} \propto p_{\text{ext}}/T$, where T is the effective temperature of the gas in the cloud that combines the different velocity components the extinction depends for a given overpressure only on the square root of the external pressure ($\tau_\lambda \propto \sqrt{p_{\text{ext}}}$).

At low optical depths, the effective optical depth becomes equal to the mean optical depth

$$\tau_\lambda^{\text{eff}}(\hat{p}, \tau_\lambda \ll 1) = \langle \tau_\lambda \rangle = 4(V_{\text{cl}}/S_{\text{cl}}) \langle n_{\text{H}} \rangle (k_\lambda^{\text{ext}}/n_{\text{H}}). \quad (\text{B.6})$$

In case of highly opaque clouds, most of the light contributing to the flux density F_λ^- arises from the rim where the extinction is lowest. The optical depth close to the edge is $\tau_\lambda \approx R_{\text{cl}} (k_\lambda^{\text{ext}}/n_{\text{H}}) n_{\text{H}}(R_{\text{cl}}) 2(\pi/2 - \varphi)$. By considering

only the contributions close to the rim, the effective optical depth of a sphere becomes

$$\tau_\lambda^{\text{eff}}(\hat{p}, \tau_\lambda \gg 1) \approx 2 \ln \left\{ 2R_{\text{cl}} k_\lambda^{\text{ext}}/n_{\text{H}} n_{\text{H}}(R_{\text{cl}}) \right\} - \begin{cases} \ln 2, & \text{sphere} \\ \ln \frac{3}{4}, & \text{cylinder.} \end{cases} \quad (\text{B.7})$$

The effective extinction of a sphere and a cylinder for a wide range of overpressures are given in Fig. B.2. For high overpressure \hat{p} , the effective optical depth can be considerably lower than the corresponding mean optical depth through a comparable homogeneous cloud of the same mass.

B.2. Escape probability

The escape probability is based on the assumption that the emissivity is proportional to the density. It is given by the ratio of the luminosity escaping the cloud without being scattered or absorbed to the total luminosity produced in the cloud

$$p_{\text{esc}}(\hat{p}, \tau_\lambda) = \frac{F_\lambda^-(\hat{p}, \tau_\lambda)}{F_\lambda^-(\hat{p}, 0)}, \quad (\text{B.8})$$

where

$$F_\lambda^-(\hat{p}, 0) = V_{\text{cl}} 4\pi (\eta_\lambda/n_{\text{H}}) \langle n_{\text{H}} \rangle / S_{\text{cl}} \quad (\text{B.9})$$

and

$$F_\lambda^-(\hat{p}, \tau_\lambda) = \int d\Omega \mathbf{n}_F \cdot \mathbf{n}_J \int_0^\infty dl \eta_\lambda(l, \Omega) \times \exp \left\{ - \int_0^l dl' k_\lambda^{\text{ext}}(l', \Omega) \right\}. \quad (\text{B.10})$$

For the sphere, the escape probability becomes

$$p_{\text{esc}}^{\text{sph}}(\hat{p}, \tau_\lambda) = \frac{3}{2 \langle n_{\text{H}} \rangle} \int_0^{\pi/2} d\vartheta \sin \vartheta \cos \vartheta \times \int_{-\cos \vartheta}^{\cos \vartheta} dl n_{\text{H}}(R_{\text{cl}} \sqrt{l^2 + \sin^2 \vartheta}) e^{-\tau_\lambda(l, \sin \vartheta)}. \quad (\text{B.11})$$

and for the cylinder

$$p_{\text{esc}}^{\text{cyl}}(\hat{p}, \tau_\lambda) = \frac{2}{\pi \langle n_{\text{H}} \rangle} \int_0^{\pi/2} d\vartheta \sin \vartheta \int_0^{\pi/2} d\varphi \cos \varphi \times \int_{-\cos \vartheta}^{\cos \vartheta} dl n_{\text{H}}(R_{\text{cl}} \sqrt{l^2 + \sin^2 \varphi}) e^{-\tau_\lambda(l, \sin \varphi)}. \quad (\text{B.12})$$

where the optical depth in the exponent is given by

$$\tau_\lambda(l, \sin \vartheta) = R_{\text{cl}} (k_\lambda^{\text{ext}}/n_{\text{H}}) \int_{-\cos \vartheta}^l dl' n_{\text{H}}(R_{\text{cl}} \sqrt{l'^2 + \sin^2 \vartheta}). \quad (\text{B.13})$$

The escape probability for self-gravitating spheres and cylinders is shown in Fig. B.3. For intermediate values, the escape probability is lower than for the homogenous clouds.

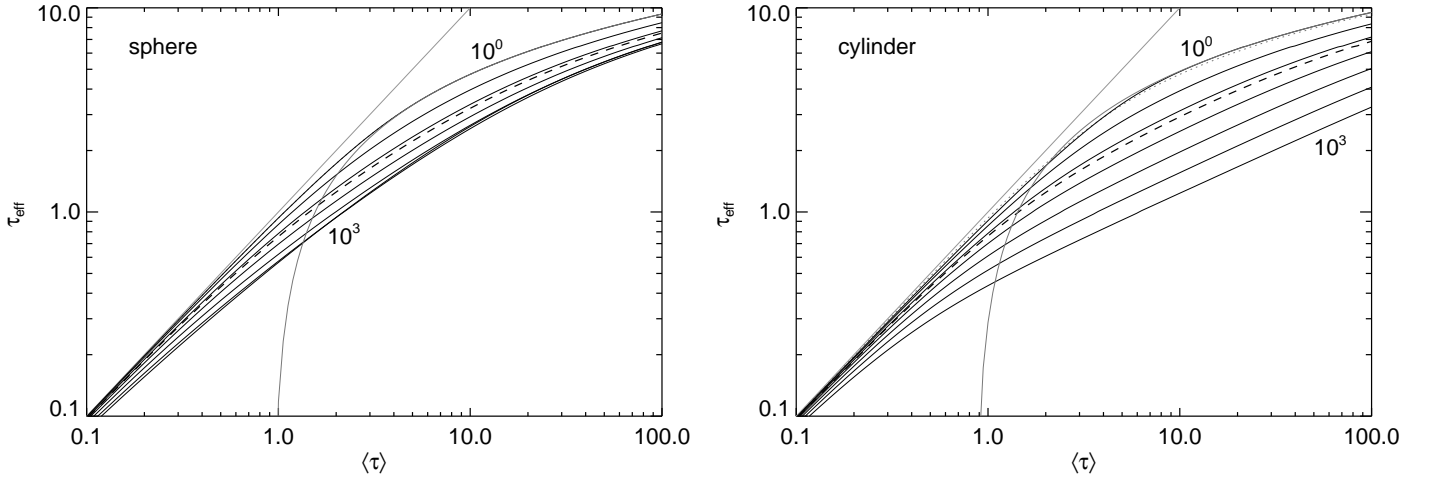


Fig. B.2. Effective optical depth of self-gravitating spheres and cylinders as function of the mean optical depth for several assumptions for the over pressure $\hat{p} = p_c/p_{\text{ext}}$. The overpressure is varied from 10^0 to 10^3 in steps of $\Delta \log \hat{p} = 0.5$. The dashed line shows the effective optical depth for clouds with over pressure $\hat{p} = 14.04$, the over pressure for critical stable spherical clouds. The thin grey lines show the approximations for low and high mean optical depths. The effective extinction of the cylinders is also compared to the corresponding values of a homogeneous sphere of the same mean optical depth (dotted line).

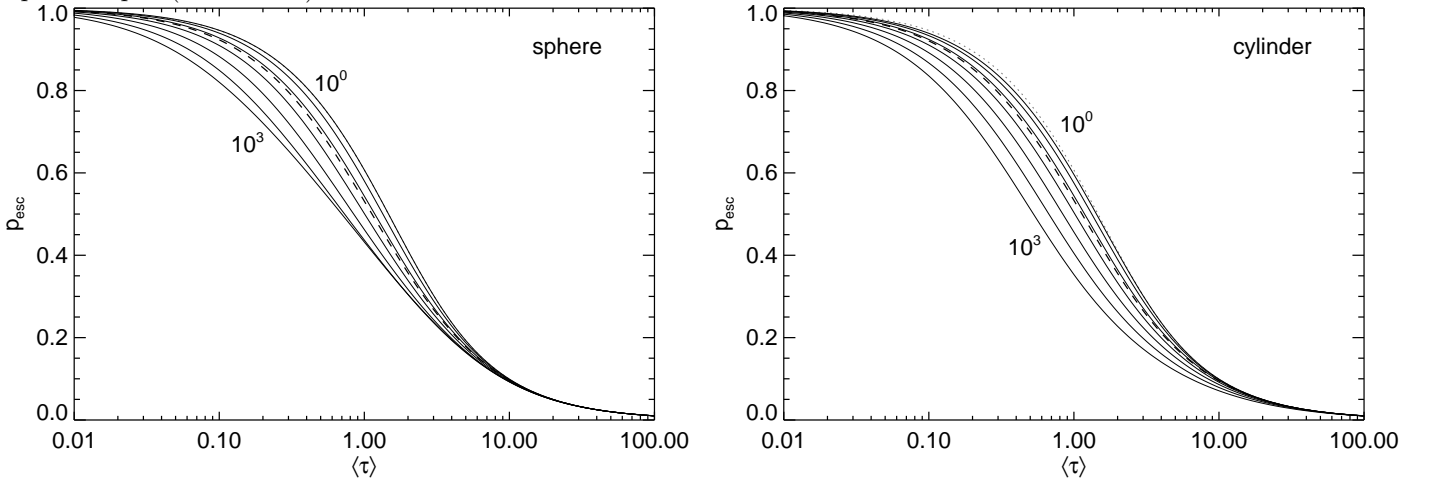


Fig. B.3. Escape probability of self-gravitating spheres and cylinders as a function of the mean optical depth. The overpressure is varied in the same range as in Fig. B.2. The dashed line shows the escape probability of a critical stable cloud with $\hat{p} = 14.04$ and dotted line in the right-hand figure the escape probability of a homogeneous sphere.

B.3. Cloud albedo

The cloud albedo is based on the escape probability described in the previous section. It is assumed that the scattered light is produced in proportion to the density. For multiple scattered events, this gives the cloud albedo

$$\omega_{\lambda}^{\text{cl}}(\hat{p}, \tau_{\lambda}) = \frac{\omega_{\lambda} p_{\text{esc}}(\hat{p}, \tau_{\lambda})}{1 - \omega_{\lambda}(1 - p_{\text{esc}}(\hat{p}, \tau_{\lambda}))}. \quad (\text{B.14})$$

These values are certainly very approximately. However, the formula indicates to first order the general way in which the cloud albedo decreases for higher extinction values. As a consequence, a larger fraction of light is absorbed inside the cloud.

References

Arendt, R. G., Odegard, N., Weiland, J. L., et al. 1998, *ApJ*, 508, 74
 Bernard, J. P., Boulanger, F., Desert, F. X., & Puget, J. L. 1992, *A&A*, 263, 258

Bernard, J. P., Boulanger, F., & Puget, J. L. 1993, *A&A*, 277, 609
 Bohlin, R. C., Savage, B. D., & Drake, J. F. 1978, *ApJ*, 224, 132
 Boisse, P. 1990, *A&A*, 228, 483
 Bok, B. J. & Reilly, E. F. 1947, *ApJ*, 105, 255
 Bonnor, W. B. 1956, *MNRAS*, 116, 351
 Boulares, A. & Cox, D. P. 1990, *ApJ*, 365, 544
 Chakrabarti, S. & McKee, C. F. 2008, *ApJ*, 683, 693
 Curry, C. L. & McKee, C. F. 2000, *ApJ*, 528, 734
 Doty, S. D., Metzler, R. A., & Palotti, M. L. 2005, *MNRAS*, 362, 737
 Draine, B. T. & Li, A. 2007, *ApJ*, 657, 810
 Dunne, L. & Eales, S. A. 2001, *MNRAS*, 327, 697
 Ebert, R. 1955, *Zeitschrift für Astrophysik*, 37, 217
 Evans, II, N. J., Rawlings, J. M. C., Shirley, Y. L., & Mundy, L. G. 2001, *ApJ*, 557, 193
 Ferrière, K. M. 2001, *Reviews of Modern Physics*, 73, 1031
 Fiege, J. D. & Pudritz, R. E. 2000a, *MNRAS*, 311, 85
 Fiege, J. D. & Pudritz, R. E. 2000b, *MNRAS*, 311, 105
 Fischera, J. 2004, *A&A*, 428, 99
 Fischera, J. & Dopita, M. 2004, *ApJ*, 611, 911
 Fischera, J. & Dopita, M. 2005, *ApJ*, 619, 340
 Fischera, J. & Dopita, M. 2008, *ApJS*, 176, 164
 Fischera, J., Dopita, M., & Sutherland, R. 2003, *ApJL*, 599, L21
 Fitzpatrick, E. L. 1999, *PASP*, 111, 63

- Gordon, K. D., Misselt, K. A., Witt, A. N., & Clayton, G. C. 2001, *ApJ*, 551, 269
- Hegmann, M. & Kegel, W. H. 2003, *MNRAS*, 342, 453
- Kauffmann, J., Pillai, T., Shetty, R., Myers, P. C., & Goodman, A. A. 2010, *ApJ*, 716, 433
- Kruegel, E. & Siebenmorgen, R. 1994, *A&A*, 288, 929
- Larson, R. B. 1981, *MNRAS*, 194, 809
- Larson, R. B. 1985, *MNRAS*, 214, 379
- Mathis, J. S., Mezger, P. G., & Panagia, N. 1982, *A&A*, 105, 372
- Netterfield, C. B., Ade, P. A. R., Bock, J. J., et al. 2009, "ApJ", 707, 1824
- Nutter, D., Stamatellos, D., & Ward-Thompson, D. 2009, *MNRAS*, 396, 1851
- Olmi, L., Ade, P. A. R., Anglés-Alcázar, D., et al. 2009, "ApJ", 707, 1836
- Ossenkopf, V. & Henning, T. 1994, *A&A*, 291, 943
- Ostriker, J. 1964, *ApJ*, 140, 1056
- Stamatellos, D. & Whitworth, A. P. 2003, *A&A*, 407, 941
- Stamatellos, D., Whitworth, A. P., André, P., & Ward-Thompson, D. 2004, *A&A*, 420, 1009
- Stodólkiewicz, J. S. 1963, *Acta Astronomica*, 13, 30
- Városi, F. & Dwek, E. 1999, *ApJ*, 523, 265
- Weingartner, J. C. & Draine, B. T. 2001, *ApJ*, 548, 296
- Witt, A. N. & Gordon, K. D. 1996, *ApJ*, 463, 681
- Witt, A. N. & Gordon, K. D. 2000, *ApJ*, 528, 799
- Wolf, S., Fischer, O., & Pfau, W. 1998, *A&A*, 340, 103